수의학박사 학위논문

Clinical Evaluation of a Modified Cardiac Computed Tomography Protocol in Dogs and Cats

개와 고양이에서 변형된 컴퓨터 단층촬영 프로토콜의 임상적 평가

2023년 8월

서울대학교 대학원

수의학과 및 임상수의학 전공

김 준 영

Clinical Evaluation of a Modified Cardiac Computed Tomography Protocol in Dogs and Cats

지도 교수 윤 정 희

이 논문을 수의학박사 학위논문으로 제출함

2023년 4월

서울대학교 대학원

수의학과 및 임상수의학 전공

김 준 영

김준영의 수의학박사 학위논문을 인준함

2023년 7월

위 원 장 _____ 최 지 혜 _____ (인)

부위원장 _____ 윤 정 희 _____ (인)

위 원 _____ 이 인 형 _____ (인)

위 원 _____ 김 민 수 _____ (인)

위 원 _____ 장 동 우 _____ (인)

Abstract

Clinical Evaluation of a Modified Cardiac Computed Tomography Protocol in Dogs and Cats

Junyoung Kim
Major in Veterinary Clinical Sciences
Department of Veterinary Medicine
The Graduate School
Seoul National University

As an alternative to invasive conventional angiography, multi-slice cardiac computed tomography (CT) has become the gold standard for non-invasive cardiovascular evaluation in human medicine. In veterinary medicine, several canine studies have reported the cardiovascular evaluation using non-electrocardiography (ECG)-gated or ECG-gated cardiac CT since 2011, but clinical applications and research are insufficient to date. Furthermore, non-ECG-gated or ECG-gated cardiac CT studies may be needed in feline medicine. Previous canine studies have indicated that ECG-gated CT methods are more effective in detailed imaging on the heart and

coronary arteries (CAs) than non-ECG-gated CT methods due to minimizing cardiac motion artifacts. However, as small animals may have a fast heart rate and beta-blockers may exhibit limited efficacy in reducing heart rates, it may be difficult to perform ECG-gating methods. Therefore, it is necessary to understand the characteristics, differences, and limitations of non-ECG-gated and ECG-gated multi-slice cardiac CT, respectively. It may also be helpful to directly compare the clinical usefulness of non-ECG-gated and ECG-gated multi-slice cardiac CT in veterinary medicine. Therefore, the present study aims to investigate the clinical applicability and limitations of the non-ECG-gated method, as well as the advantages of using exclusively ECG-gated images. This will be done by simultaneously applying both methods to dogs and cats. The ultimate goal of this study is to establish an appropriate high-slice cardiac CT scan protocol for dogs and cats, which can be utilized in the future.

In Chapter 1, non-ECG-gated and ECG-gated methods using 160-slice CT equipment were applied simultaneously to six dogs (two patent ductus arteriosus, two heart base tumors, one pericardial mesothelioma, and one normal). A total of five sequential non-ECG-gated scans were performed at 5 s intervals, followed by retrospective ECG-gated scan without bolus tracking. Images were reviewed to determine the optimal scan timing in non-ECG-gated images and R-R interval in ECG-gated images for detailed CA imaging, respectively, and the visual assessment of main CA branches was performed in the selected images. In addition, the left CA branching patterns in six dogs were classified, and morphological evaluations such as the size and margination of the lesions were compared in non-ECG-gated and ECG-gated CT images in dogs with heart or pericardial tumors. The scan timing of non-ECG-gated and the R-R interval of ECG-gated images showing optimal CA

visualization were identified as the second-scan timing and the end-diastole (R-R interval 70-90%), respectively. Non-ECG-gated, second-scan images showed high-grade in all main CA branches except the septal branch of dogs under 5 kg in visual CA assessment, and showed no significant difference from ECG-gated images. In morphological evaluation of the lesions, small-sized heart or pericardial lesions in two dogs were clearly identified in ECG-gated images compared to non-ECG-gated images. This study demonstrates that non-ECG-gated high-slice CT method is capable of evaluating the main CAs in dogs. However, it also suggests that ECG-gated CT method should be preferred over non-ECG-gated method for identifying small-sized lesions in the heart or pericardium.

In Chapter 2, the same cardiac CT scan method as in Chapter 1 was used to evaluate the feline CAs. A total of six cats (five normal, one hypertrophic cardiomyopathy phenotype) were included in the study. The characteristics of five sequential non-ECG-gated CT images were described according to scan timing. The optimal scan timing in non-ECG-gated images and R-R interval in ECG-gated images for detailed CA imaging were selected, and the visual assessment of main CA branches was performed in the selected image. In addition, coronary dominance and the left CA branching types were classified, and the correlation between the diameter / length of each CA branch and body weight, sex, and vertebral heart scores (VHS) were evaluated as well. In non-ECG-gated method, the first-scan images exhibited good opacification of the cranial vena cava (CrVC), right ventricular outflow tract (RVOT), and pulmonary arteries in all cats. However, imaging of the left heart and CAs proved to be difficult. The second-scan images were found to be the most suitable for opacifying the left heart and CAs, although they only allowed imaging of the coronary ostium and proximal branches due to severe motion artifacts. The

opacification of the left heart and CAs in the third-scan images was lower compared to the second-scan images. The fourth and fifth-scan images could not be evaluated due to contrast medium washout. On the other hand, in ECG-gated CT images, the visualization of CAs was rated as good to excellent, with a detailed course at the end-diastole. These images were significantly superior to the non-ECG-gated images in all cats. Additionally, variable patterns of coronary dominance and left CA branching types could be identified. The length and diameter of CAs showed no significant correlation with body weight and sex, but VHS showed a positive correlation with right CA length and negative correlation with left main CA. In conclusion, the new (modified) cardiac CT scan protocol in this study was successfully performed in all cats. It is believed that this scanning method may be beneficial for the simultaneous evaluation of the CrVC, RVOT, and pulmonary arteries, as well as the left heart and CAs. This may aid in the assessment of patients with congenital cardiovascular anomalies such as pulmonic stenosis (PS) or left persistent cranial vena cava (CrVC), enabling a comprehensive evaluation of both sides of the heart.

In Chapter 3, it was designed to identify variations in the diameter of the pulmonary vein (PV) ostium throughout the cardiac cycle and assess the benefits of utilizing ECG-gated CT images obtained with a new (modified) cardiac CT scan protocol. The ECG-gated CT images in Chapter 2 were reviewed retrospectively to investigate the number of PV ostium, PV drainage patterns, the diametric variations of PV ostium according to the cardiac cycle, and the correlation between the size of heart / left atrium (LA) and PV ostial diameter. In all cats, 3 PV ostia, including right cranial ostium, left cranial ostium, and caudodorsal ostium, were identified, showing 2 drainage patterns into LA and the diametric variations of PV ostium according to the cardiac cycle. The maximal diameter of each PV ostium was identified at the end-

systole and the minimal diameter at the end-diastole. Statistical analysis also confirmed that there was a significant difference in PV ostial diameter between the end-systole and end-diastole ($p<0.05$). No significant correlation was found between the size of heart / LA and 3 PV ostial diameter ($p>0.05$). This study showed that the ECG-gated cardiac CT images are useful for providing detailed PV anatomy, including the diametric variations of the feline PV ostium according to the cardiac cycle. In addition, the present study may provide the potential research on the effects of PV ostium on variable patterns of feline pulmonary edema and atrial fibrillation, and may increase the possibility of clinical application to interventional procedures such as radiofrequency ablation in veterinary clinics in future. This study demonstrates the benefits of exclusively utilizing ECG-gated images with the new (modified) cardiac CT scan protocol, providing evidence of PV ostial changes according to the cardiac cycle.

In conclusion, this new (modified) cardiac CT scan method, non-ECG-gated scan followed by subsequent ECG-gated scan without bolus tracking, allowed successful cardiac scanning in dogs and cats, showing potential benefits of reducing radiation exposure and anesthesia time. The non-ECG-gated high-slice cardiac CT scan method shows clinical utility by allowing evaluation of the main CAs in dogs. It can also be combined with imaging of the CrVC, RVOT, and pulmonary arteries, aiding in the assessment of both sides of the heart in patients with congenital cardiovascular diseases such as PS or left persistent CrVC. Additionally, the ECG-gated scan method offers advantages in identifying small-sized lesions in the heart or pericardium, as well as evaluating feline CAs and changes in the PV ostium throughout the cardiac cycle. Overall, the new (modified) cardiac CT scan protocol holds promise as a reliable and practical tool for clinical application in veterinary

medicine, supporting the assessment and management of various cardiovascular conditions in dogs and cats.

Keywords: electrocardiography, computed tomography, coronary artery, pericardium, pulmonary vein, cardiac cycle

Student Number: 2018-38660

Table of Contents

List of Abbreviations

BW	body weight
CA	coronary artery
CDO	caudodorsal ostium
CI	confidence interval
CM	castrated male
Cr	cranial
CrVC	cranial vena cava
CS	coronary sinus
CT	computed tomography
CTA	computed tomographic angiography
ECG	electrocardiography
HCM	hypertrophic cardiomyopathy
LA	left atrium
LCA	left coronary artery
LMCA	left main coronary artery
LO	left cranial ostium
MDCT	multidetector computed tomography
MIP	maximum intensity projection
MPR	multiplanar projection
NT-proBNP	N-terminal pro-B-type natriuretic peptide

PA	pulmonary artery
PDA	persistent ductus arteriosus
PS	pulmonic stenosis
PV	pulmonary vein
RCA	right coronary artery
RCO	right cranial ostium
RO	right cranial ostium
RPV	right pulmonary vein
RV	right ventricle
RVOT	right ventricular outflow tract
SD	standard deviation
SF	spayed female
VHS	vertebral heart score
VR	volume-rendered
3D	three-dimensional

List of Figures

List of Tables

General Introduction

With the rapid development of multi-slice computed tomography (CT), various non-invasive cardiovascular evaluations using cardiac CT have been conducted in human medicine. These include the diagnosis of coronary artery (CA) disease, pre-operative screening or follow-up after surgery for CA disease, and guidance for interventional procedures such as radiofrequency ablation through pulmonary vein (PV) evaluation in patients with atrial fibrillation (Cao *et al.*, 2019; Drees *et al.*, 2011b; de Heer *et al.*, 2012; Manghat *et al.*, 2012; Taron *et al.*, 2019; Lei *et al.*, 2015; Lacomis *et al.*, 2007; Ratajczak *et al.*, 2016; Hassani & Saremi, 2017). Cardiac CT scans can be performed using non-electrocardiography (ECG)-gating or ECG-gating (prospective or retrospective) methods (Drees *et al.*, 2014; Nagpal *et al.*, 2020). In prospective ECG-gated scans, image acquisition is only triggered during a certain phase of the cardiac cycle, commonly at the end-diastolic phase, during which the heart is mostly motionless (Drees *et al.*, 2014; Nagpal *et al.*, 2020). This is favored for morphological evaluations, as adequate image quality is provided at a lower radiation dose relative to non-ECG-gated and retrospective ECG-gated scans. However, prospective scans do not acquire a full-cycle dataset; further, in patients with irregular heart rhythms or higher heart rates, prospective scans may lead to the acquisition of an incomplete dataset and may fail to capture the optimal phase of the cardiac cycle during diastole. In retrospective scans, image acquisition is triggered over the entire length of one or more cardiac cycles, and the dataset can be retrospectively separated into different phases of the cardiac cycle (usually in 5–10%

intervals). Thus, cardiac function and morphology can be evaluated in different phases of the cardiac cycle, and images can depict the beating heart over the entire cardiac cycle (Drees *et al.*, 2014; Nagpal *et al.*, 2020). For small animals with fast heart rates, the retrospective method may be more useful than the prospective method. On the other hand, the non-ECG-gating method is a technique where rapid and multiple sequential back-to-back scanning over the cardiac silhouette is performed without the need for bolus tracking or a test bolus (Gunther-Harrington *et al.*, 2019). Although the non-ECG-gating method may have lower image resolution in detailed cardiac anatomy compared to the ECG-gating method, it offers the advantages of fast scanning and the ability to image without being affected by the patient's heart rate and heart rhythm. As a result, the non-ECG-gating method may be a suitable choice for patients with rapid heart rates or arrhythmias, as it allows for easy imaging without being influenced by these factors. Several veterinary studies using the non-ECG-gating or ECG-gating method have reported that the ECG-gating method is superior to the non-ECG-gating method because it can minimize cardiac motion artifacts (Visser *et al.*, 2013; Laborda-Vidal *et al.*, 2015; 2016; Gunther-Harrington *et al.*, 2019; Stieger-Vanegas *et al.*, 2019; To *et al.*, 2019). However, as most of these studies have been used 64-slice or less CT equipment, there remains a need of clinical application and research on non-ECG-gated or ECG-gated method using high-slice CT equipment in veterinary medicine. Recently, the use of high-performance CT equipment (more than 64-slice) has been increasing in veterinary clinics. Therefore, it is necessary to understand the advantages and characteristics of the non-ECG-gating or ECG-gating method using high-slice CT equipment, i.e., more than 64-slice CT. In particular, research on cardiac CT is needed in feline medicine. This study aimed to pursue the appropriate cardiac CT scan method and

its clinical application by simultaneously applying the non-ECG-gating and retrospective ECG-gating methods using high-slice CT in dogs and cats with or without cardiac diseases. First, it aimed to evaluate the imaging characteristics and differences between two methods: non-ECG-gating and ECG-gating. Second, a comparative evaluation of CA anatomy between two methods in dogs and cats was conducted. Third, a retrospective analysis of ECG-gated images in cats was performed to assess the advantages of the ECG-gated method, specifically investigating the anatomical features of the PV ostium, including changes in PV ostial diameter according to the cardiac cycle. This study hypothesized that the ECG-gated method provides advantages for evaluating CAs compared to the non-ECG-gated method. Additionally, it was expected that the ECG-gated method would enable the identification of changes in the diameter of the PV ostium in accordance with the cardiac cycle.

Chapter 1. Clinical Utility of a Modified Cardiac CT Protocol in Dogs

1.1 Introduction

As an alternative to invasive conventional angiography, multidetector computed tomography (MDCT) angiography is the gold standard for non-invasive cardiovascular evaluation in humans (Drees *et al.*, 2011b; de Heer *et al.*, 2012; Manghat *et al.*, 2012; Taron *et al.*, 2019). Further, several veterinary studies have described cardiovascular evaluation using electrocardiography (ECG)- or non-ECG-gated MDCT. ECG-gated MDCT is superior to non-ECG-gated MDCT in terms of imaging the cardiac morphology and the detailed coronary artery (CA) courses because it minimizes cardiac motion artifacts (Visser *et al.*, 2013; Laborda-Vidal *et al.*, 2015; 2016; Gunther-Harrington *et al.*, 2019; Stieger-Vanegas *et al.*, 2019). However, it may be difficult to apply the ECG-gating method to patients with rapid heart rates or arrhythmias; furthermore, the use of beta-blockers to reduce the heart rate in dogs, which may be necessary for cardiac MDCT, has limited efficacy and given rise to potential complications (Drees *et al.*, 2011b). Therefore, understanding the characteristics of non-ECG-gated MDCT in veterinary clinics is necessary. Moreover, ECG-gated imaging has the disadvantage of increased anesthesia time and radiation exposure, which requires a test bolus or a bolus-tracking method to yield the optimal delay time (Drees *et al.*, 2014).

Most canine studies using non-ECG-gated MDCT have applied 4-, 8-, 16-, or 64-slice MDCT. To date, only one report detailed the case of a Boston Terrier diagnosed

with combined pulmonic stenosis and aberrant CA using non-ECG-gated 160-multislice MDCT (Kim *et al.*, 2021). Therefore, the advantages or characteristics of non-ECG-gated imaging through advanced high-slice MDCT using more than 64 slices in veterinary clinics remain unclear. As technology continues to advance, high-performance equipment employing 640-slice MDCT is being used more frequently in human medicine (Lei *et al.*, 2015; Cao *et al.*, 2019). Thus, advanced high-slice MDCT using more than 64 slices may eventually become more commercially available in veterinary medicine. Further, cardiac evaluation using high-performance MDCT may be clinically feasible for reducing anesthesia time and improving image resolution. A canine study using 256-slice MDCT evaluated two-dimensional left ventricular measurements based on the cardiac cycle in retrospective ECG-gated imaging (Kim *et al.*, 2019). However, other cardiac structures, including the CA, remain to be evaluated. Another study used non-ECG-gated 16-slice and ECG-gated 64-slice MDCT to successfully obtain diagnostic images of canine cardiac anatomy (Saulnier, 2012). Nevertheless, its clinical application was limited by the need for the use of beta-blockers or alpha-2 agonists, which can induce bradycardia (Saulnier, 2012). Few studies have directly compared the characteristics of non-ECG- and ECG-gated imaging using high-slice cardiac CT with more than 64 slices in veterinary clinics.

Therefore, this study aimed to investigate and compare the clinical utility and limitations of non-ECG- and ECG-gated high-slice cardiac CT in dogs with and without heart disease. Moreover, it was also aimed to establish the relevant clinical applications of high-slice cardiac CT based on individual patient history.

1.2 Materials and Methods

1.2.1 Animals

This was an observational study. The medical records were retrospectively searched at Helix Animal Medical Center for dogs that underwent non-ECG- and ECG-gated 160-multislice CT angiography between 2020 and 2021. All examinations were performed as part of standard clinical practice. The care, maintenance, and study design followed protocols approved by the Institutional Animal Care and Use Committee at Seoul National University (approval number: SNU-220106-2). Informed consent was obtained from the owners of all dogs prior to any procedures being performed.

1.2.2 Anesthesia

For all dogs, an intravenous 22- or 24-G catheter was placed in the right or left cephalic vein for premedication and contrast agent injection during MDCT. All dogs were pre-medicated using butorphanol (0.2 mg/kg intravenous; 1 mg/mL, Butophan®; Myungmoon Pharm Co., Ltd., Seoul, Republic of Korea). General anesthesia was induced using propofol (6 mg/kg intravenous; 10 mg/mL, Provive® 1%; Myungmoon Pharm Co., Ltd.) and maintained using isoflurane (Isotroy® 100; Troikaa Pharmaceuticals Ltd., Gujarat, India) after orotracheal intubation. During anesthesia induction, non-invasive blood pressure, heart rate, oxygen saturation, and end-tidal carbon dioxide level were continuously monitored through ECG, pulse oximetry and capnography. Data acquisition began approximately 5–10 min after anesthesia induction to ensure the stability of the anesthetic conditions. For individual scans, apnea was induced through hyperventilation using the breath-

holding technique immediately prior to the scan.

1.2.3 Non-ECG-and ECG-gated cardiac CT technique

MDCT angiography was performed using an 80-row, 160-multislice CT system (Aquilion Lightning®; Canon Medical Systems Co., Otawara, Japan). All dogs were positioned in sternal recumbency on a CT table with the neck extended and the forelimbs caudally placed. ECG leads were attached to the paws, and ECG was simultaneously recorded during spiral MDCT examination. The scan parameters were as follows: voltage, 120 kilovoltage peak (kVp); gantry speed, 0.5 s/rotation; slice collimation, 0.5 × 80 mm; 150 mA; 0.5-mm slice thickness; and pitch factor, 0.813. All dogs underwent non-ECG-gated scanning, followed by retrospective ECG-gated scanning after a short break to allow washout of the contrast medium. For non-ECG-gated scanning, biphasic injection, which involved 1.5 mL/kg non-ionic contrast medium (300 mg/I/mL, Omnipaque®; GE Healthcare, Seoul, Republic of Korea) followed by a saline flush (1.5 mL/kg, 0.9% NS®; Dai Han Pharm Co., Ltd., Seoul, Republic of Korea) was administered into the cephalic vein using a dual power injector (OptiVantage™ DH; Mallinckrodt, Dublin, Ireland) at a rate of 1.5 mL/s. After 8 s of contrast injection, contrast cardiac CT scans from the second sternum to the cranial border of the diaphragm were repeated at five times.

To reduce radiation exposure and anesthesia time, the delay time for retrospective ECG-gated scanning was determined using non-ECG-gated scan images. The contrast medium for ECG-gated MDCT was administered similar to that for non-ECG-gated MDCT. During post-processing data manipulation, the images were reconstructed in multiple datasets with an increase in the temporal reconstruction

window at 10% increments within the cardiac cycle, which was centered over the 0–90% R-R interval. The dataset with the least motion artifact was selected for further post-processing. All images were reviewed by two veterinary diagnostic imaging experts (Junyoung Kim, Siheon Lee) using specialized software (Vitrea 7.12®; Vital Images, Minnetonka, MN, USA) at a dedicated viewing station (Figure 1).

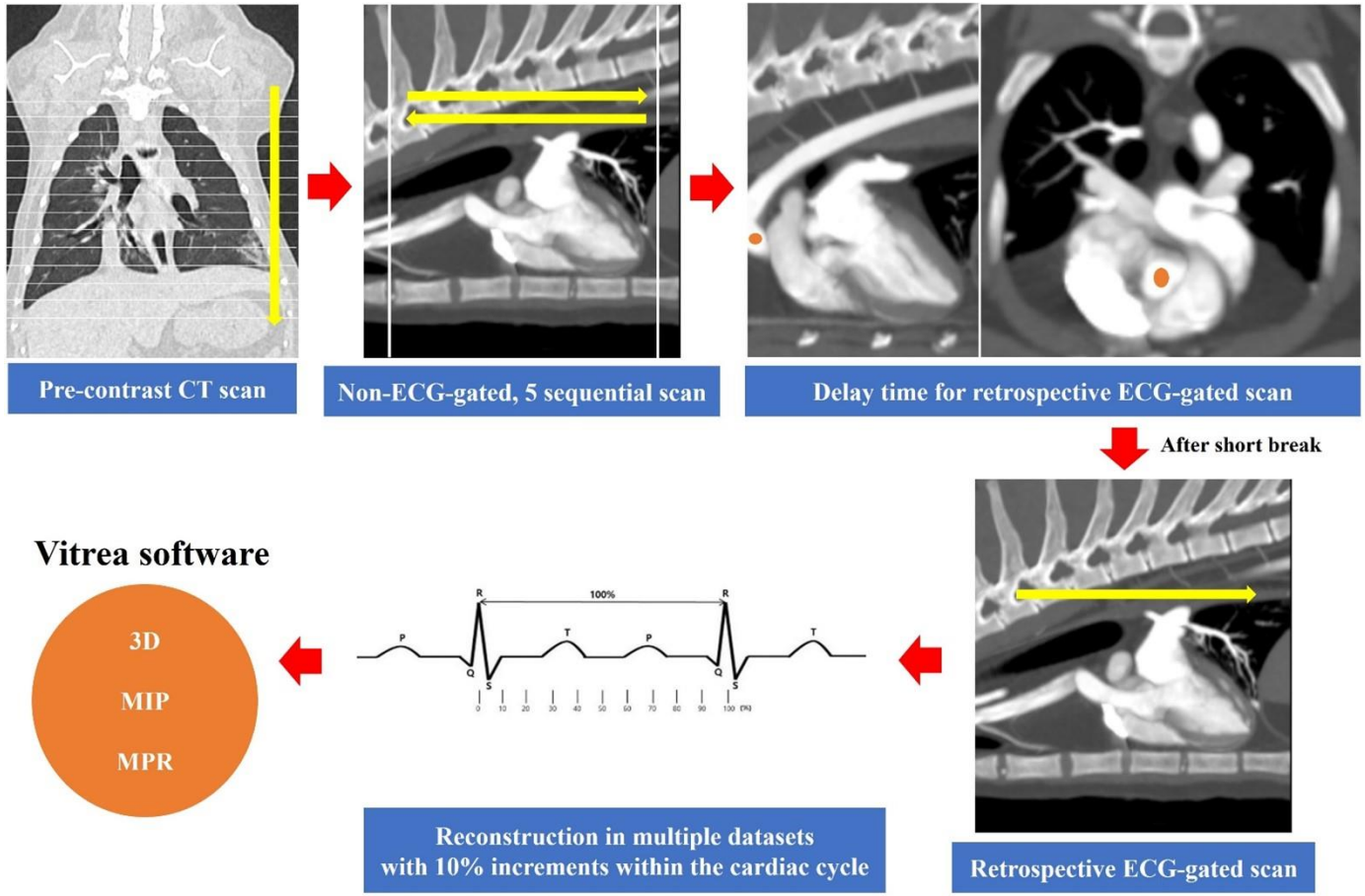

Figure 1. The cardiac computed tomography (CT) scan method used in this study. All dogs were examined using non-electrocardiography (ECG)-

gated scans, followed by ECG-gated scans. First, a pre-contrast CT scan of the full thorax from the thoracic inlet to the caudal-most border of the lungs was performed prior to the post-contrast studies. For non-ECG-gated scans, five sequential scans, cranial to caudal and vice versa, from the second rib to the cranial border of the diaphragm, were performed at 5-s intervals. The delay time for retrospective ECG-gated scans was determined based on non-ECG-gated sequential images. After that, retrospective ECG-gated scan was performed. For data post-processing, images were reconstructed in multiple datasets, with the temporal reconstruction window increasing in 10% increments within the cardiac cycle, centered over the 0–90% R-R interval. Maximum intensity projection (MIP), three-dimensional (3D) volume-rendered (VR), and multiplanar reconstructions were applied as needed.

1.2.4 Evaluation of non-ECG-gated and ECG-gated 160-multislice MDCT images

The optimal scan timing and R-R interval in non-ECG- and ECG-gated images were determined for the detailed cardiac anatomy, including the CA, that allowed minimum motion artifacts. The images using MIP, 3D VR, multiplanar, and curved reconstructions for optimal CA visualization were compared.

Further, the diagnostic quality of the optimal CA visualization was evaluated and compared in the selected optimal non-ECG- and ECG-gated images through visual assessment of the main CA branches—namely, the circumflex (Cx), paraconal interventricular (Pc), septal (S), and the right CA. The CA visual assessment was subjectively graded by the two above-mentioned experts as poor (0), mild (1), good (2), or excellent (3) (Figure 2). Images graded as poor to mild and good to excellent were considered low- and high-grade images, respectively. Images were graded by consensus, and both readers concurred in all cases.

The subtypes of the left CA (LCA) branching pattern were classified as previously described (Auriemma *et al.,* 2018) (Figure 3). In type I, the three major branches (i.e., the Pc, Cx, and S branches) arise from a short common trunk after its aortic origin. In type 2, the common trunk serves as the origin of the Cx and Pc branches, while the S branch directly arises from the Pc. In type 3, there is no common trunk, with the Cx and Pc branches originating from the left sinus of Valsalva as two distinct vessels, and the S branch arising from the Cx branch shortly after its origin. In type 4, three major divisions arise from a short common trunk as in type 1; however, an additional efferent vessel, which is arbitrarily named as the intermediate Pc branch, originates from the Pc branch shortly after its origin. In type 5, there is no common trunk, with the Cx and Pc branches distinctly originating as in type 3 and the S branch

arising from the Pc. In type 6, the Pc, Cx, and S branches originate from the short common trunk, while an additional S branch arises from the Pc.

Finally, the size and margin demarcation of the heart or pericardial lesions in patients with heart or pericardial tumors were compared using non-ECG- and ECG-gated images.

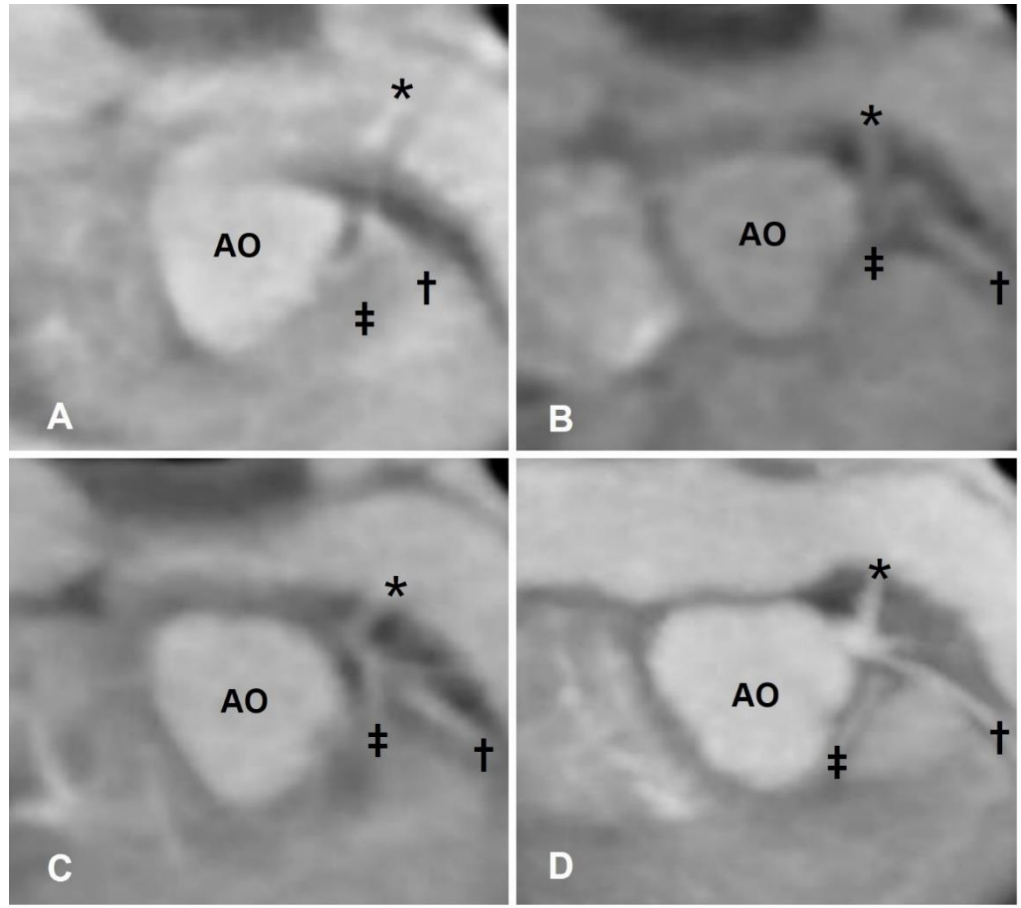

Figure 2. Visual assessment of the canine coronary arteries in non-electrocardiography (ECG)-gated 160-slice multidetector computed

tomography images. (A) 0 (poor): poor opacification of the coronary branches with severe blurring, which impedes the evaluation of the coronary arteries at their origin. (B) 1 (mild): adequate opacification of the origins of the coronary arteries, allowing evaluation; however, the coronary courses cannot be diagnostically evaluated due to moderate blurring. (C) 2 (good): adequate opacification and sharpness of the coronary branches with an acceptable degree of blurring, but possible presence of mild artifacts; the origins of the coronary arteries and distal branches can be evaluated. (D) 3 (excellent): excellent opacification and sharpness of the coronary branches, with few artifacts. AO, aorta; ⋆, circumflex; †, paraconal interventricular; ‡, septal.

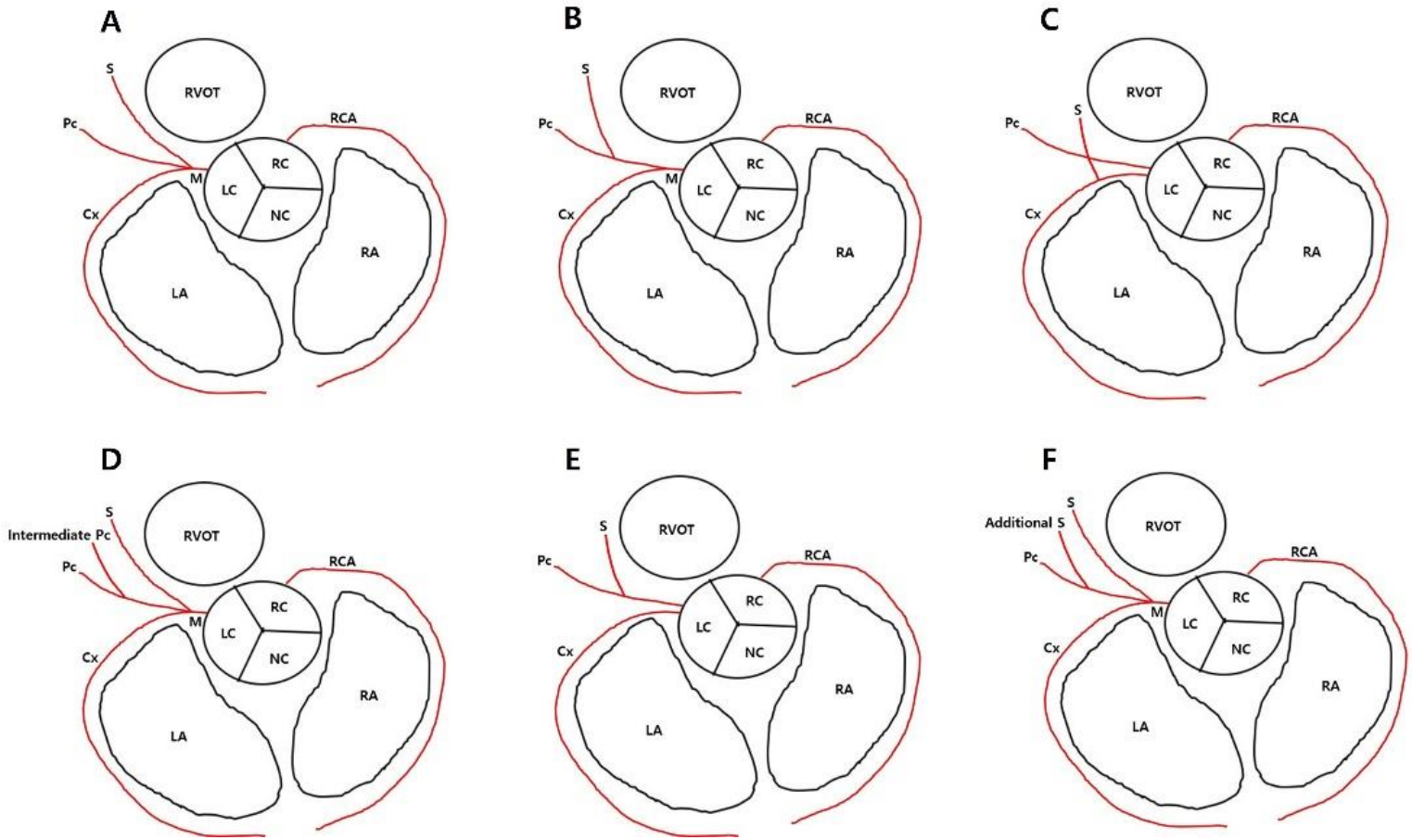

Figure 3. Types of left coronary artery branching in dogs. (A) Type I: the three major branches, paraconal interventricular (Pc), circumflex (Cx),

and septal (S) branches, arise from a short common trunk (M) after its aortic origin. (B) Type 2: M serves as the origin of the Cx and Pc branches, while the S branch directly arises from the Pc. (C) Type 3: there is no M, with the Cx and Pc branches originating from the left sinus of Valsalva as two distinct vessels, and the S branch arising from the Cx branch shortly after its origin. (D) Type 4: three major divisions arise from M as in type 1; however, an additional efferent vessel, which is arbitrarily named as the intermediate Pc branch, originates from the Pc branch shortly after its origin. (E) Type 5: there is no M, with the Cx and Pc branches distinctly originating as in type 3 and the S branch arising from the Pc. (F) Type 6: the Pc, Cx, and S branches originate from M, while an additional S branch arises from the Pc. LA: left atrium; LC: left coronary cusp; NC: noncoronary cusp; RA: right atrium; RC: right coronary cusp; RCA: right coronary artery; RVOT: right ventricular outflow tract.

1.2.5 Statistical analyses

Data are expressed as means ± standard deviations (SDs). Fisher's exact test was used to analyze grade data regarding the imaging quality of each coronary branch, including in the reference, non-ECG, and ECG groups. A virtual reference group was established using cases with non-cardiac CT images. The imaging quality grade of the reference group was assumed to be 0. The P-value for between-group comparisons was adjusted using Bonferroni correction. Statistical analyses were performed using R software version 4.0.4. Statistical significance was set at $P < 0.05$.

1.3 Results

Six dogs (one Bichon Frise, one Maltese, one Pomeranian, one Pompitz, one Shetland Sheepdog, and one Fox Terrier), including two spayed females and four neutered males, were included in this study (Table 1). The mean age and body weight (BW) of the dogs were 63.2 ± 46.5 months and 7.1 ± 4.1 kg, respectively. Of the six dogs, two had patent ductus arteriosus classified as type IIA, as previously described (Miller *et al.*, 2006), two had heart base tumors, one had pericardial mesothelioma, and one had normal heart check-up findings (Table 1). All patients underwent thoracic radiography, echocardiography, and laboratory examinations prior to the MDCT scan. The dog with normal findings underwent the MDCT scan upon the owner's request for a detailed cardiac evaluation, including the CA. The diagnosis of patent ductus arteriosus in two dogs was confirmed via a surgical approach. One dog with heart base tumor (Case 1) was tentatively diagnosed with pericardial mesothelioma based on cytological examination of the pericardial effusion and MDCT findings. The other dog with a heart base tumor (Case 5) was tentatively diagnosed with an aortic body chemodectoma or ectopic thyroid tumor based on cytological examination of the heart base mass and MDCT findings. Pericardial mesothelioma was confirmed in one dog (Case 4) through histological examination of the pericardial lesions obtained through pericardiectomy.

The range of heart rates during the MDCT scan was 90–130 bpm. None of the dogs showed complications related to the anesthetic protocol. In all dogs, second-scan images in non-ECG-gated MDCT revealed maximal contrast enhancement at the proximal ascending aorta. Therefore, the delay time for retrospective ECG-gated scans, which was approximately 15 s, could be determined using the second-scan

images in non-ECG-gated scans.

In ECG-gated MDCT images, the optimal interval for CA evaluation was the end-diastolic phase at 70–90% R-R interval (Table 2). There were wide variations in the LCA branching patterns, with two, one, one, and two cases of types 1, 2, 5, and 6, respectively (Table 2). None of the dogs showed aberrant CAs.

Second-scan images of non-ECG-gated MDCT allowed high-grade (good to excellent) visualization for most CA branches in the visual assessment, without a large difference from ECG-gated MDCT images (Table 3). However, the S branch and right CA in three dogs and one dog, respectively, showed low-grade (poor to mild) visualization (Table 3). Compared with the reference group, the ECG group showed significantly high imaging quality in all CA branches, while the non-ECG group showed significantly high imaging quality in all CA branches except the S branch (Table 4). Compared with non-ECG-gated images, ECG-gated images showed insignificantly high imaging quality of all CA branches in all dogs (Table 4).

Table 1. Characteristics and history of the six included dogs

Case	Breed	History	Age (months)	Sex	BW (kg)
1	Maltese	Heart base tumor	117	CM	4.4
2	Pomeranian	PDA	26	SF	4.0
3	Bichon Frise	PDA	8	CM	3.2
4	Pompitz	Pericardial mesothelioma	60	SF	7.0
5	Fox Terrier	Heart base tumor	120	CM	10.4
6	Shetland Sheepdog	Cardiac check-up	48	CM	13.6

BW, body weight; CM, castrated male; PDA, persistent ductus arteriosus; SF, spayed female.

Table 2. Optimal R-R interval for visualizing the coronary arteries with the least motion artifacts in electrocardiography (ECG)-gated 160-multislice computed tomography and corresponding left coronary artery (LCA) branching patterns in six dogs

Case	Optimal R-R interval in ECG-gated scan	LCA branching pattern
1	70%	Type 1
2	80%	Type 1
3	90%	Type 5
4	70%	Type 2
5	80%	Type 6
6	70%	Type 6

ECG, electrocardiography; LCA, left coronary artery.

Table 3. Comparative evaluation of diagnostic quality based on the imaging of the main coronary artery (CA) branches using non-electrocardiography (ECG)- and ECG-gated 160-multislice computed tomography in dogs

Case	Cx		Pc		S		Right CA	
	Non-ECG	ECG	Non-ECG	ECG	Non-ECG	ECG	Non-ECG	ECG
1	3	3	3	3	0	1	1	2
2	2	3	2	3	0	3	3	3
3	2	3	2	3	0	1	2	3
4	2	2	2	2	2	2	2	2
5	2	3	3	3	2	3	3	3
6	3	3	3	3	3	3	2	3

0 = poor, 1 = mild, 2 = good, 3 = excellent.
CA, coronary artery; Cx, circumflex; ECG, electrocardiography; Pc, paraconal interventricular; S, septal.

Table 4. P-values for between-group comparisons of each coronary artery (CA) branch[a]

CA branch	R[b] vs. Non-ECG	R vs. ECG	Non-ECG vs. ECG	Total
Cx	.006	.006	.73	< .001
Pc	.006	.006	1	< .001
S	.55	.006	.47	.004
RCA	.006	.006	1	< .001

CA, coronary artery; Cx, circumflex; ECG, electrocardiography; Pc, paraconal; R, reference group; RCA, right coronary artery; S, septal.
[a]P values for between-group comparisons were adjusted using Bonferroni correction.
[b]A virtual reference group using cases with non-cardiac computed tomographic images was set up. The imaging quality grade of the reference group was set at 0 for among-group comparisons.

Implementation of 3D VR in non-ECG-gated MDCT images allowed the evaluation of all LCA branches in five of the six dogs, except for the S branch in three dogs (Figure 4). This could be attributed to the low-grade images of the S branch. This is supported by the fact that non-ECG-gated images of the S branches in the other two dogs were well imaged in 3D VR images. Additionally, 3D VR could not be implemented in one dog with pericardial mesothelioma because of excessive pericardial effusion.

The evaluation of the size and margination of the heart or pericardial lesions in Case 1 (heart base tumor) and Case 4 (pericardial mesothelioma) clearly revealed small pericardial nodules in the ECG-gated MDCT images, which were not clearly identified in the non-ECG-gated MDCT images (Figures 5 and 6).

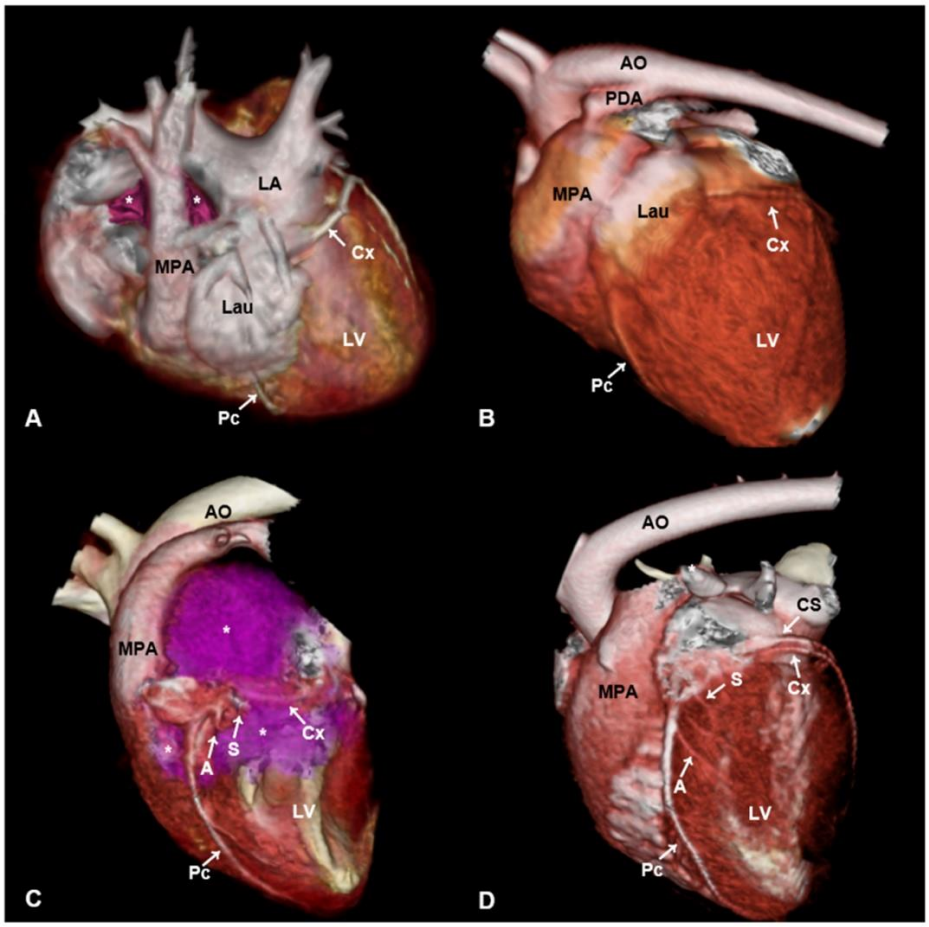

Figure 4. Three-dimensional volume-rendered images in non-electrocardiography-gated 160-multislice computed tomography. Images from Cases 1 (A) and 3 (B) show excellent depictions of the paraconal interventricular (Pc) and circumflex (Cx) coronary branches; however, the septal branch could not be identified due to inadequate opacification. Images from Cases 5 (C) and 6 (D) present good depictions of the septal, additional septal, Pc, and Cx branches in two dogs with the type 6 left coronary artery branching pattern. (D) Image showing the coronary sinus (CS) in a normal dog. The purple asterisks in (A) and (C) indicate the heart base tumors in the two dogs. A, additional septal branch; AO, aorta; LA, left atrium; Lau, left auricle; LV, left ventricle; MPA, main pulmonary artery; RV, right ventricle.

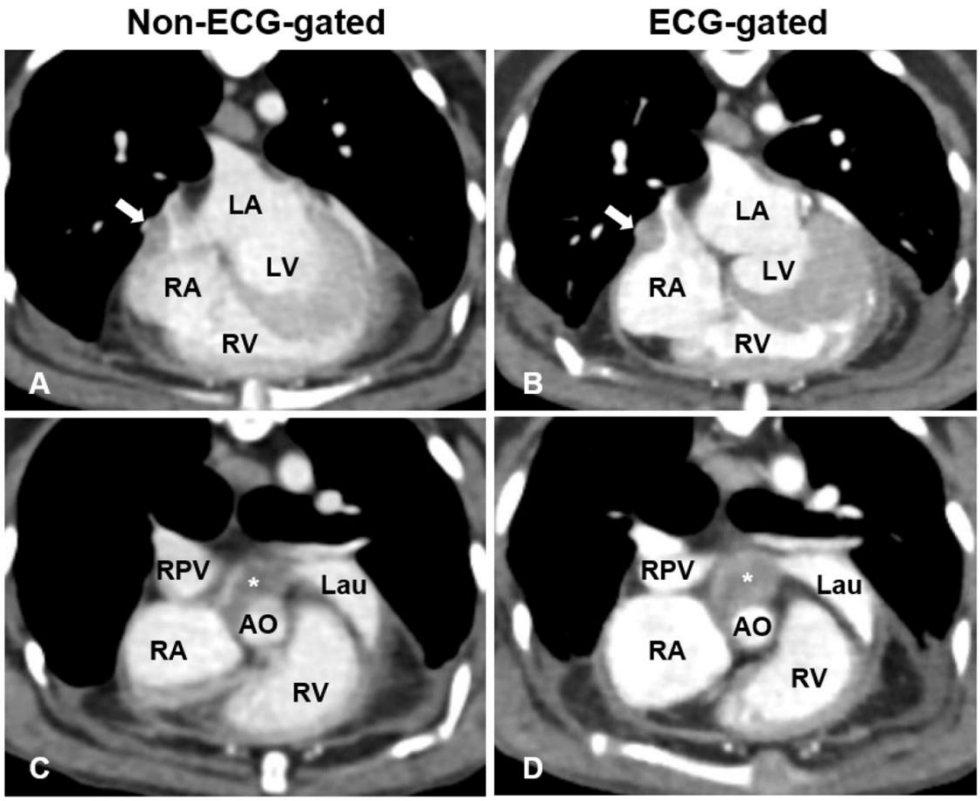

Figure 5. Comparative evaluation of non-electrocardiography (ECG)- and ECG-gated images using 160-multislice computed tomography in a dog (Case 1) with a heart base tumor. The ECG-gated image, but not the non-ECG-gated image, clearly reveals a small pericardial nodule (arrows) (A, B). The size of the heart base tumor (asterisks) was 12.62 mm × 8.86 mm and 14.93 mm × 10.16 mm in non-ECG- and ECG-gated images, respectively, indicating that the mass is larger and more sharply demarcated in the ECG-gated image than in the non-ECG-gated image (C, D). AO, aorta; LA, left atrium; Lau, left auricle; RA, right atrium; RPV, right pulmonary vein; RV, right ventricle.

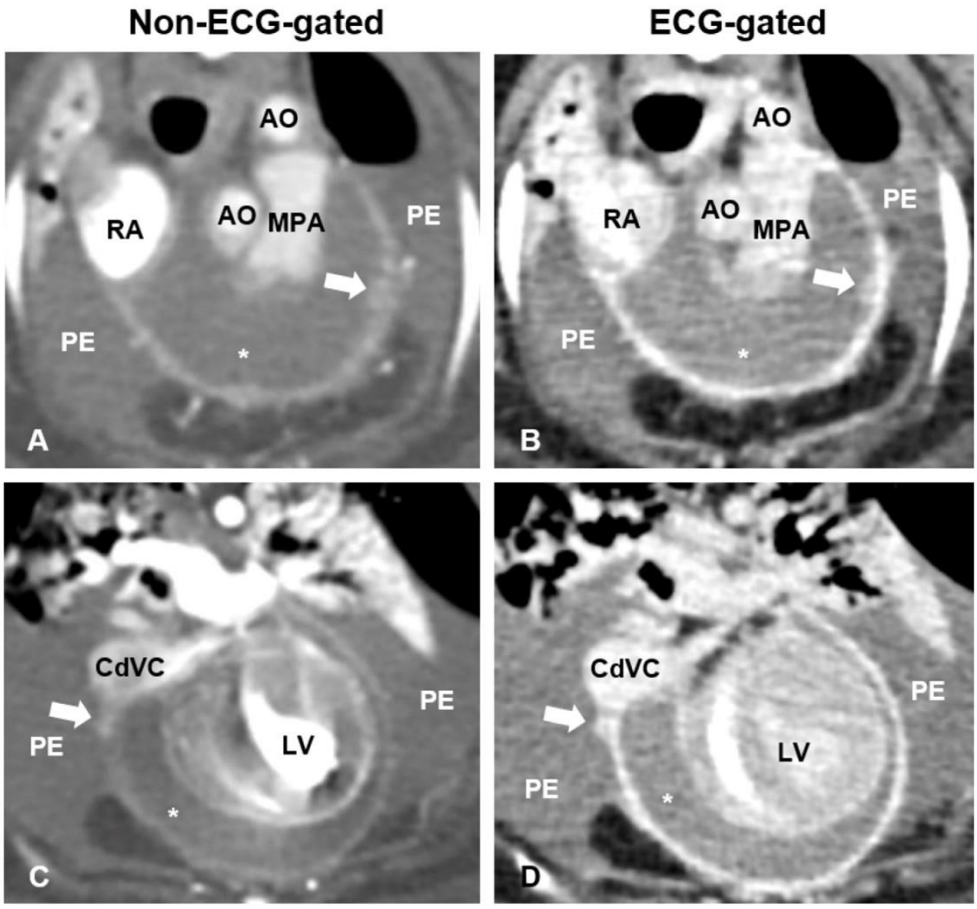

Figure 6. Comparative evaluation of non-electrocardiography (ECG)- and ECG-gated images using 160-multislice computed tomography in a dog (Case 4) with pericardial mesothelioma. The ECG-gated images (B, D), but not the non-ECG-gated images (A, C), clearly reveal two small pericardial nodules (arrows). The asterisks indicate pericardial effusion. AO, aorta; CdVC, caudal vena cava; LV, left ventricle; MPA, main pulmonary artery; PE, pleural effusion; RA, right atrium; RPV, right pulmonary vein.

1.4 Discussion

This study describes the characteristics and differences of non-ECG- and ECG-gated cardiac CT methods using 160-multislice equipment in various canine breeds. With the non-ECG-gated method, the second-scan images showed high-grade imaging quality with regard to the visual assessment of all main CA branches, except the S branch, in dogs weighing <5 kg. The lower image quality in small dogs was attributed to the relatively smaller diameter of the S branch compared with the other CA branches. These results are consistent with those of a previous report noting the relatively small diameter of the S branch and a positive correlation between BW and CA diameter (Auriemma *et al.*, 2018). Nonetheless, given the high-grade imaging quality of the origin and detailed courses of all other CA branches, and that S branch abnormalities remain to be reported, CA anomalies can be identified and classified using only the non-ECG-gated method of high-slice MDCT (Scansen, 2017). Furthermore, studies on anomalies of the single coronary ostium confirm that these anomalies may increase CA diameter, which makes it more apparent on MDCT images (Kim *et al.*, 2021; Owens *et al.*, 2021).

Compared with non-ECG-gated images, ECG-gated MDCT images allowed better visual assessment of all main CA branches, although the difference was not significant. This suggests that for evaluating the CA, the non-ECG-gated method is as good as the ECG-gated technique. Moreover, a 70–90% interval (end-diastolic phase) was the optimal R-R interval of the cardiac cycle for CA visualization. This could be attributed to maximal coronary blood flow and less cardiac motion during the end-diastolic phase, which is consistent with findings from previous studies (Drees *et al.*, 2011b; 2014; Auriemma *et al.*, 2018). Additionally, various LCA

branching patterns were identified, consistent with those identified in previous reports (Drees *et al.*, 2011b; Auriemma *et al.*, 2018).

Of interest, in Case 1, ECG-gated MDCT images of the heart base mass showed a sharper boundary with larger sizes than non-ECG-gated images (Figure 4). These findings suggest that ECG-gated MDCT images have prominent advantages with respect to reducing cardiac motion artifacts. In Case 5, there was no difference in the heart mass size between non-ECG- and ECG-gated images, which could be attributed to the mass being of a size sufficient to remain unaffected by cardiac motion artifacts.

This study indicates that ECG-gated cardiac CT images clearly identify small-sized pericardial nodules in dogs. In fact, authors could identify and diagnose these nodules in ECG-gated images, but not in non-ECG-gated images. Identifying these nodules allowed biopsy with pericardiectomy in one dog with pericardial mesothelioma. In another dog with a heart base tumor, precise size measurement of the heart base mass with clear demarcation of the margin and the small pericardial nodule could be performed. In contrast, there was no significant difference in size and margins between non-ECG- and ECG-gated MDCT images in another dog with a heart base tumor, which could be attributed to the large mass size and fewer cardiac motion artifact effects.

This study presents the first scan protocol involving setting the delay time between non-ECG-gated images and subsequent ECG-gated images without bolus tracking or a test bolus, which allowed successful ECG-gated scanning. Although this modified scan method was used to directly compare non-ECG- and ECG-gated high-slice MDCT images in the same dogs, it conferred the additional advantage of reducing radiation exposure. Further, widening of the fourth or fifth scan range may

be considered for cases requiring examination of the abdomen or whole body. Therefore, this modified scan method could prove clinically useful in evaluating tumoral metastasis in patients with cancer.

This study has some limitations. First, the sample size was small, and histopathological examination was not performed in two dogs (Cases 1 and 5) with heart base masses due to lack of consent for biopsy. However, although not able to determine the nature of the heart base mass, this study demonstrated the advantages and disadvantages of ECG- and non-ECG-gated cardiac CT images. Additionally, evaluation with non-ECG-gated high-slice MDCT imaging appears to be necessary for dogs with fast or irregular heart rates.

Despite the limitations, this study suggests clinical significance in veterinary medicine. New (modified) cardiac CT scan protocol in this study could allow whole-body or abdominal examination and detailed imaging of cardiac anatomy with reduced anesthesia time and radiation exposure. Moreover, this study suggests that non-ECG-gated high-slice cardiac CT scans should be considered a viable option for reducing anesthesia time in patients requiring CA evaluation. Additionally, ECG-gated cardiac CT scan is appropriate for patients with suspected intracardiac or pericardial tumors. This study can facilitate significant advancements, including the development of individualized high-slice cardiac MDCT scanning and its applications based on patient history.

Chapter 2. Clinical Utility of a Modified Cardiac CT Protocol in Cats

2.1 Introduction

MDCT angiography is considered the gold standard for evaluating coronary vessels in humans, permitting multiple interventional cardiologic procedures as well as providing valuable information to predict the extent and prognosis of CA disease (Shah *et al.*, 2012; Chen *et al.*, 2014; Punzo *et al.*, 2019; Stieger-Vanegas *et al.*, 2019; Sun, 2012). The main applications of cardiac CT in human medicine are demonstrated in the detection and assessment of degree of coronary stenosis and prediction of disease outcome (Sun, 2012). Although CA stenosis, reported commonly in humans, rarely occurs in animals, various congenital or acquired coronary diseases have been reported in veterinary medicine (Piffer *et al.*, 1994; Fernandez *et al.*, 1997; Drees *et al.*, 2011b; Scansen, 2017; Stieger-Vanegas *et al.*, 2019). Anomalous CAs in combination with pulmonic stenosis have been reported predominantly in dogs (Drees *et al.*, 2011b; Scansen, 2017; Stieger-Vanegas *et al.*, 2019). In cats, a morphological alteration has been observed that has also been reported in the long-tailed chinchilla, where the right CA is usually missing and only a single CA exists (Barszcz *et al.*, 2017). Recently, a domestic shorthair cat diagnosed with a congenital coronary cameral fistula, with the right coronary artery to the left ventricle communication, has been reported (Bowden *et al.*, 2022). Such knowledge may be especially helpful in explaining the pathophysiology of CA diseases (Barszcz *et al.*, 2017). Therefore, understanding the anatomy, terminology,

and clinical implications of these CA anomalies is critical for the diagnosis and treatment of veterinary patients. Moreover, it has been reported that cats exhibit variable morphological variations of the CA (Scansen, 2017). However, there has been only one reported case regarding the evaluation of CA using cardiac CT in feline medicine (Bowden *et al*., 2022). This may be attributed to technical difficulties in imaging caused by the fast heart rate of cats and the lack of high-performance CT equipment. Nevertheless, the utilization of high-performance CT equipment in veterinary clinics has recently increased.

Previous reports on canines indicated that ECG-gated MDCT was more effective in identifying anomalous CAs than non-ECG-gated MDCT in terms of imaging the cardiac morphology and the detailed CA courses due to minimized cardiac motion artifacts (Visser *et al.*, 2013; Laborda-Vidal *et al.*, 2016; Gunther-Harrington *et al.*, 2019; Stieger-Vanegas e*t al.*, 2019). Although ECG-gated CT has the advantage of being able to control cardiac motion artifacts, animals have faster heart rates than humans, and beta-blockers exhibit limited efficacy in reducing heart rates in animals (Drees *et al*., 2011b). A recent study successfully diagnosed a CA anomaly using non-ECG-gated, high-slice cardiac CT (Kim *et al.*, 2021). Therefore, it is essential to consider the necessity and usefulness of non-ECG-gated CT imaging (Drees *et al.*, 2011b). However, there is a paucity of research directly comparing the clinical feasibility of ECG-gated and non-ECG-gated MDCT for evaluating feline CAs (Drees *et al.*, 2011b; Saulnier, 2012; Laborda-Vidal *et al.*, 2016; Gunther-Harrington *et al.*, 2019). Therefore, this study was conducted to investigate the characteristics and differences between non-ECG-gated and ECG-gated imaging using high-slice CT equipment in cats, as well as to describe the anatomy of feline CAs and evaluate the clinical applicability of CA evaluation. Ultimately, the main goal of this study

was to establish an appropriate high-slice cardiac CT scan protocol for cats.

2.2 Materials and Methods

2.2.1 Animals

This study was a prospective, controlled, comparative pilot study including cats that had been brought to the Helix Animal Medical Center for a complete medical check-up. The study design, as well as animal care and maintenance, followed protocols approved by the Institutional Animal Care and Use Committee of Seoul National University (approval number: SNU-220113-4). Medical history and informed consent were obtained for all client-owned cats prior to the study procedures. Six domestic short-haired cats with no clinical signs provided by the owners were included. Before the MDCT examination, all cats underwent basic health tests, including physical examination, complete blood count, serum biochemistry, and electrolyte tests. N-terminal pro-B-type natriuretic peptide (NT-proBNP) testing, thoracic radiography, and transthoracic echocardiography (Aplio 500®, Canon Medical Systems) were performed for cardiac evaluation. Using thoracic radiography, the vertebral heart score (VHS) was calculated. Two-dimensional, M-mode, and Doppler ECG examinations were performed on all cats. The time interval between all basic health tests and MDCT examinations for individual cat was within five days.

2.2.2 Anesthesia

An intravenous 24-G catheter was placed in the right cephalic vein for premedication and contrast agent injection during MDCT. The cats were pre-medicated with butorphanol (0.2 mg/kg intravenously; 1 mg/mL, Butophan®; Myungmoon Pharm Co., Ltd.), and general anesthesia was induced with propofol (6

mg/kg intravenously; 10 mg/mL, Provive® 1%, Myungmoon Pharm Co., Ltd.) and maintained with isoflurane (Isotroy® 100, Troikaa Pharm Ltd.) in a gas mixture of 100% oxygen via an endotracheal tube. End-tidal carbon dioxide levels were maintained between 35–45 mmHg using a mechanical ventilator. Heart rate, oxygen saturation, and end-tidal carbon dioxide were continuously monitored during anesthesia using ECG, pulse oximetry and capnography. Data acquisition was initiated within 5–10 min after induction of anesthesia to ensure the stability of anesthetic conditions. For individual scan, apnea was induced by breath-holding at inspiration immediately before the scan. All cats were monitored until recovery from anesthesia. The total time from the start to the end of anesthesia was recorded.

2.2.3 Non-ECG- and ECG-gated cardiac CT technique

MDCT CA angiography was performed using an 80-row, 160-multislice CT system (Aquilion Lightning®, Canon Medical Systems). For both non-ECG-gated and ECG-gated MDCT, all cats were positioned in sternal recumbency on a CT table with the neck extended and the forelimbs positioned caudally. ECG leads were attached to the paws; ECG data were recorded simultaneously during spiral MDCT examination. Scan parameters were as follows: voltage, 120 kVp; gantry speed, 0.5 s/rotation; slice collimation, 0.5 mm × 80; 150 mA; 0.5 mm slice thickness; and pitch factor, 0.813. All cats were examined using non-ECG-gated scans, followed by ECG-gated scans after a short interval (5 min) to allow the contrast medium to wash out from the heart (Figure 1). In all cats, a pre-contrast MDCT scan of the full thorax from the thoracic inlet to the caudal-most border of the lungs was performed prior to the post-contrast studies. For non-ECG-gated scans, a biphasic injection was administered, comprising a non-ionic contrast medium (1.5 mL/kg; 300 mg/I/mL,

Omnipaque®; GE Healthcare), followed by a saline flush (1.5 mL/kg, 0.9% NS®; Dai Han Pharm Co., Ltd.) into the cephalic vein using a dual power injector (OptiVantage™ DH, Mallinckrodt) at a rate of 1.5 mL/s. Image acquisition began 8 s after the initiation of the contrast injection. Subsequently, five sequential scans, cranial to caudal and vice versa, from the second rib to the cranial border of the diaphragm, were performed at 5-s intervals. To reduce radiation exposure and anesthesia time, the delay time for retrospective ECG-gated scans was determined based on non-ECG-gated sequential images. Contrast medium administration for ECG-gated MDCT was conducted in the same manner as that for non-ECG-gated scans. For data post-processing, images were reconstructed in multiple datasets, with the temporal reconstruction window increasing in 10% increments within the cardiac cycle, centered over the 0–90% R-R interval. All images were reviewed by three veterinary diagnostic imaging experts (Junyoung Kim, Kitae Kim, Dayoung Oh) on a dedicated viewing station using specialized software (Vitrea 7.12®, Vital Images).

2.2.4 Comparative evaluation of non-ECG-gated and ECG-gated images

All images obtained in the non-ECG-gated and ECG-gated MDCT examinations were evaluated, and the characteristics of five sequential non-ECG-gated CT images were described according to scan timing. The optimal scan timing and R-R interval in non-ECG- and ECG-gated images were determined for the detailed CA anatomy that allowed minimum motion artifacts. The images using MIP, 3D VR, multiplanar, and curved reconstructions for optimal CA visualization were compared.

Further, the diagnostic quality of the optimal CA visualization was evaluated and compared in the selected optimal non-ECG- and ECG-gated images through visual assessment of the main CA branches—namely, the circumflex (Cx), paraconal

interventricular (Pc), septal (S), and the right CA. The CA visual assessment was subjectively graded as poor (0), mild (1), good (2), or excellent (3) (Figure 7). Images graded as poor to mild and good to excellent were considered low- and high-grade images, respectively.

2.2.5 Criteria for CA analysis

The ECG-gated images were assessed based on the following:

(a) coronary dominance (right, left, or codominance), which was defined as a left CA (LCA) or right CA (RCA) extending beyond the crux cordis (intersection between the interatrial, subsinosus interventricular, and coronary sulci) and the origin of the subsinosal interventricular branch (de Oliveira *et al.*, 2011; Auriemma *et al.*, 2018).

(b) classification of LCA branching into five main types of the LCA proximal segment, as previously described (Figure 8) (Barszcz *et al.*, 2017). Type I branching was characterized by a double-branched left main CA (LMCA), giving rise to the Cx and Pc branches, which branched off to the S branch. Type II was characterized by a double-branched LMCA, giving rise to the Cx and Pc branches without an S branch. Type III was characterized by a triple-branched LMCA, giving rise to the Cx, Pc, and S branches. Type IV was characterized by a double-branched LMCA, giving rise to the Pc and Cx, which branched off to the S branch. Type V was characterized by the lack of an LMCA and two separate ostia for the Cx and Pc originating from the aorta.

(c) the diameter and length of the LCA and RCA according to the segmentation of their branches, based on a method used in previous canine studies (Figure 9) (Drees *et al.*, 2011a; Auriemma *et al.*, 2018). The maximum vessel diameter was measured

at the origin of each coronary branch. The summed length of each left coronary branch, defined as total LCA herein, was then calculated.

2.2.6 Statistical analyses

All data are expressed as means ±SDs. Fisher's exact test was used to analyze grade data regarding the imaging quality of each coronary branch, including in the reference, non-ECG, and ECG groups. A virtual reference group was established using cases with non-cardiac CT images. The imaging quality grade of the reference group was assumed to be 0. The P-value for between-group comparisons was adjusted using Bonferroni correction. Statistical analyses were performed using GraphPad Prism 9.0.2 software (GraphPad Software, San Diego, CA, USA). Data were assessed for conformance to a normal distribution using the Shapiro-Wilk test. Linear correlations of BW, sex, and VHS with the diameter and length of the major coronary branches were identified using Pearson's chi-squared test. Pearson's correlation coefficients, 95% confidence intervals (CIs), and P-values were calculated for each contrast. The mean values of sex-related parameters were compared using a two-tailed unpaired Student's *t*-test. P-values < 0.05 were considered statistically significant.

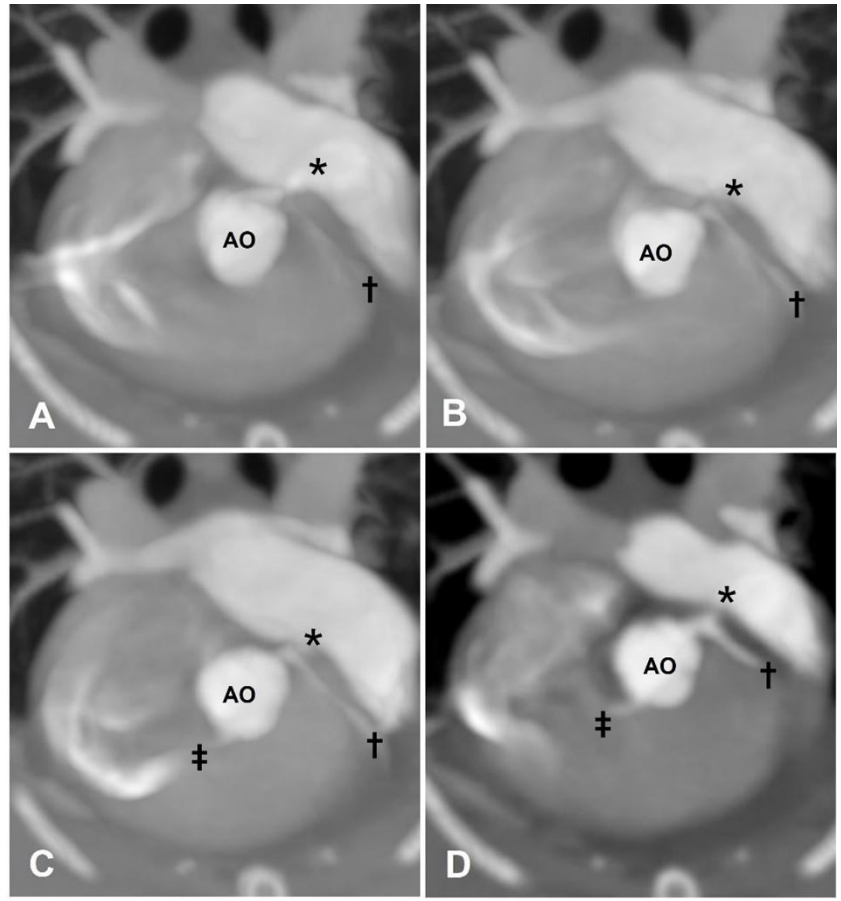

Figure 7. Degree and sharpness of feline coronary arteries in electrocardiography (ECG)-gated computed tomographic images. (A) 0 (poor): poor

opacification of the coronary branches with severe blurring prohibiting the evaluation of coronary arteries at their origins. (B) 1 (mild): origins of coronary arteries with adequate opacification can be evaluated but are non-diagnostic for evaluating the course of coronary arteries with moderate blurring. (C) 2 (good): adequate opacification and sharpness of coronary branches with an acceptable degree of blurring, where mild artifacts may be present, but origins of coronary arteries and distal branches can be evaluated. (D) 3 (excellent): excellent opacification and sharpness of coronary branches with minimal artifacts. AO: aorta; ⋆: circumflex; †: paraconal interventricular; ‡: right coronary artery.

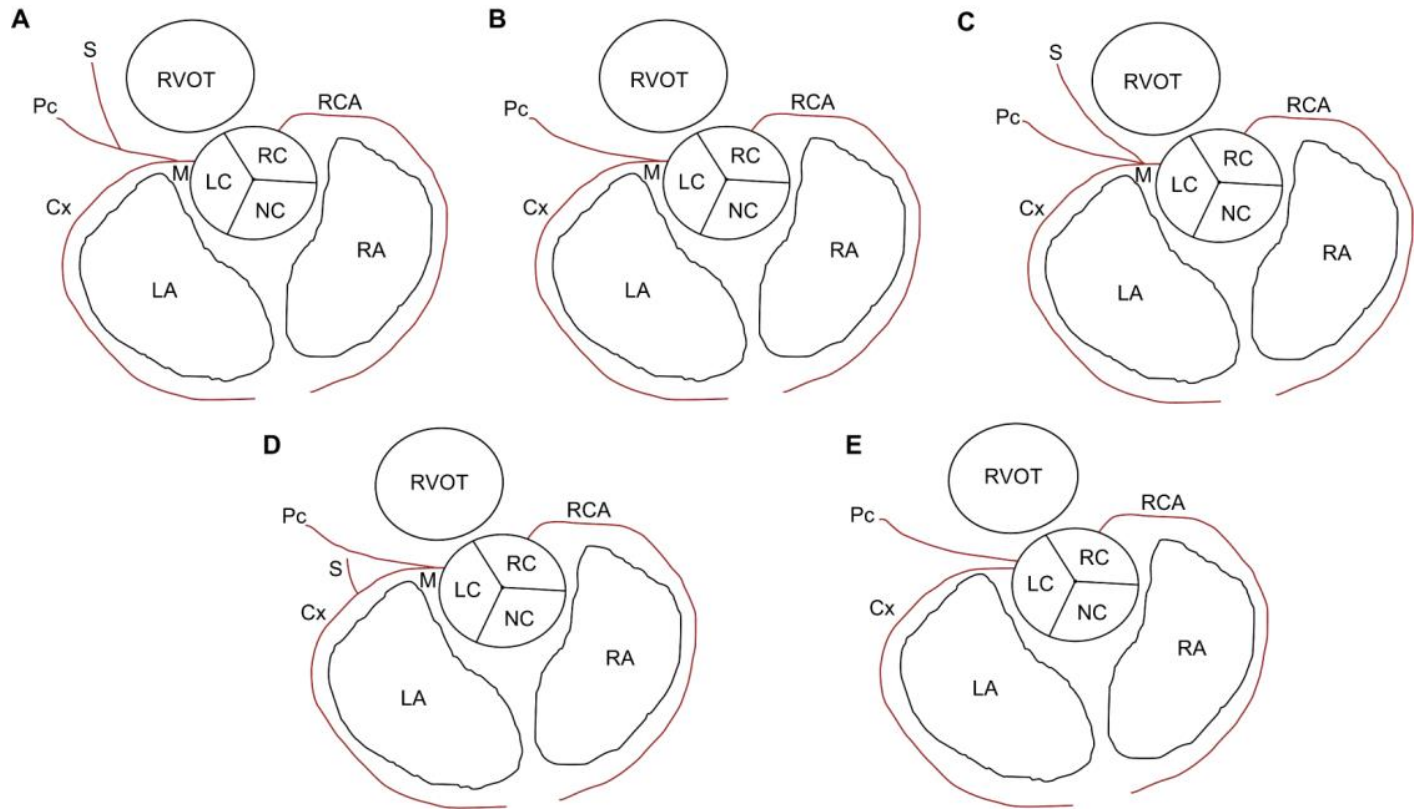

Figure 8. Types of left coronary artery branching in cats (Barszcz *et al*., 2017). (A) Type I: short left main coronary artery (M) giving rise to the circumflex (Cx) branch and paraconal interventricular (Pc) branch, which branches off to the septal (S) branch. (B) Type II: M gives rise to the

Cx and Pc branches without an S branch. (C) Type III: M gives rise to the Cx, Pc, and S branches. (D) Type IV: M gives rise to the Pc branch and Cx branch, which branches off to the S branch. (E) Type V: no M and two separate ostia for Cx and Pc branches originating from the aorta. LA: left atrium; LC: left coronary cusp; NC: noncoronary cusp; RA: right atrium; RC: right coronary cusp; RCA: right coronary artery; RVOT: right ventricular outflow tract.

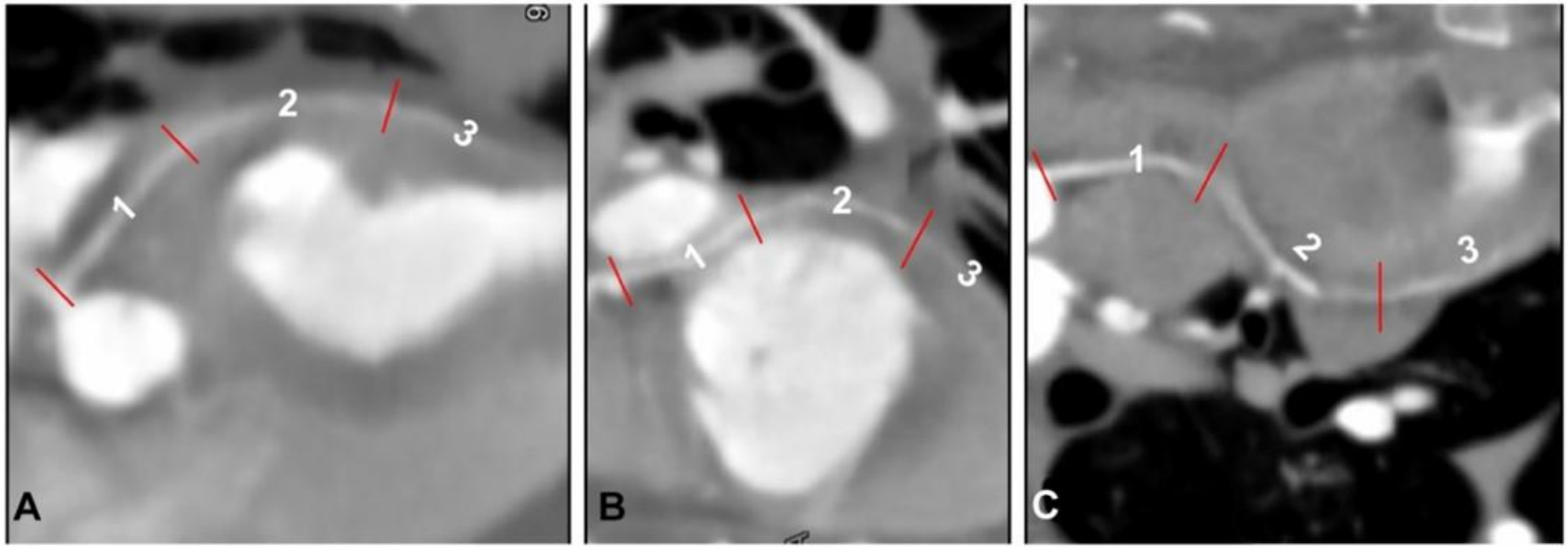

Figure 9. Segmentation of the paraconal interventricular (Pc) branch (A), circumflex (Cx) branch (B), and right coronary artery (RCA) (C) classified by adapting a previously described segmental coding system (Auriemma *et al.*, 2018), displayed as curved multiplanar reconstruction.

2.3 Results

2.3.1 Animals and feasibility of a new (modified) cardiac CT protocol

The six cats included (mean age, 4.85 ± 3.74 years; mean BW, 4.82 ± 1.00 kg; mean VHS, 7.03 ± 0.72 v) comprised three spayed females and three males (one intact and two neutered) (Table 5). Five cats exhibited normal results in all basic health tests. One cat (Case 6) was diagnosed with hypertrophic cardiomyopathy (HCM) phenotype and had a positive NT-proBNP test result (Table 5), with a systemic blood pressure of 150 mmHg and a normal serum thyroid hormone concentration of 2.1 μg/dL (reference range, 0.6–3.9 μg/dL).

A new (modified) cardiac CT protocol using non-ECG-gated and ECG-gated scans was performed successfully on all cats. The average total time from the induction of anesthesia to the conclusion of MDCT examination was 30 min (range, 25–35 min) per cat. Heart rates during the MDCT scan were 120–150 bpm in all cats. No complications associated with the anesthetic protocol were documented. The delay time for the retrospective ECG-gated scan, determined using the second-scan images for non-ECG-gated scanning, was set at 14 s in all cats (figure 10).

Table 5. Results of the signalment, vertebral heart scale (VHS), left atrium (LA) to aorta (AO) ratio, and N-terminal pro-B-type natriuretic peptide (NT-proBNP) in six domestic short-haired cats.

Case No.	Age (years)	Sex	BW (kg)	VHS	LA/AO	NT-proBNP
1	3.0	SF	4.14	7.2 v	1.44	Negative
2	3.6	M	4.24	6.0 v	1.37	Negative
3	1.0	SF	4.40	7.2 v	1.11	Negative
4	2.7	SF	4.48	6.9 v	1.00	Negative
5	8.0	CM	6.80	6.7 v	1.13	Negative
6	10.8	CM	4.85	8.2 v	1.56	Positive

BW, body weight; CM, castrated male; M, intact male; SF, spayed female.

2.3.2 Comparative evaluation and selection of optimal coronary images of non-ECG- and ECG-gated images

In non-ECG-gated images, the first-scan images exhibited no contrast enhancement in the left heart, which precluded the evaluation of the left heart and CAs in all cats (Figure 10). However, good opacification of the cranial vena cava (CrVC), right ventricular outflow tract (RVOT), pulmonary arteries (PAs) was identified in all cats (Figure 11). The second-scan images were found to be the most suitable for opacifying the left heart and CAs, although they only allowed imaging of the coronary ostium and proximal branches with blurring, streaking, and stair-stepping caused by cardiac motion artifacts. Therefore, a detailed assessment of the course of the CA was not feasible in all cats except for the Pc branch in case 6 (Figure 12, Table 6). The opacification of the left heart and CAs in the third-scan images was possible, but it was lower compared to the second-scan images. In the fourth and fifth scan images, it was not possible to evaluate the images due to poor opacification caused by the wash-out of the contrast medium, resulting in unsuitable images. (Figure 10).

In ECG-gated images, all CA branches were more clearly identified compared to non-ECG-gated images (Table 6,7). In ECG-gated images, the optimal R-R reconstruction intervals for both the LCA and RCA were 70, 80, and 90% in two, one, and three cases, respectively (Table 8). In line with previous canine investigations, the CAs in all cats were best visualized during the late end-diastolic phase, when the coronary flow is expected to be maximal and cardiac motion is reduced. Common artifacts included blurring and stair-step appearance secondary to cardiac motion. These artifacts were more frequently observed in non-ECG-gated images than in ECG-gated images. In selected ECG-gated images, the degree of

opacification and sharpness of the proximal coronary branches was subjectively evaluated as excellent (3/6; 50%) or good (3/6; 50%) in all cats (Table 6). ECG-gated images also enabled the characterization of the course of coronary branches based on diagnostic images in all cats. The S branch was identified in only two cats, which limited the ability to conduct statistical evaluation. In the statistical analysis, compared with the reference group, the ECG group showed significantly high imaging quality in all CA branches, while the non-ECG group showed insignificantly high imaging quality in all CA branches (Table 7). Compared with non-ECG-gated images, ECG-gated images showed significantly high imaging quality of all CA branches in all dogs (Table 7).

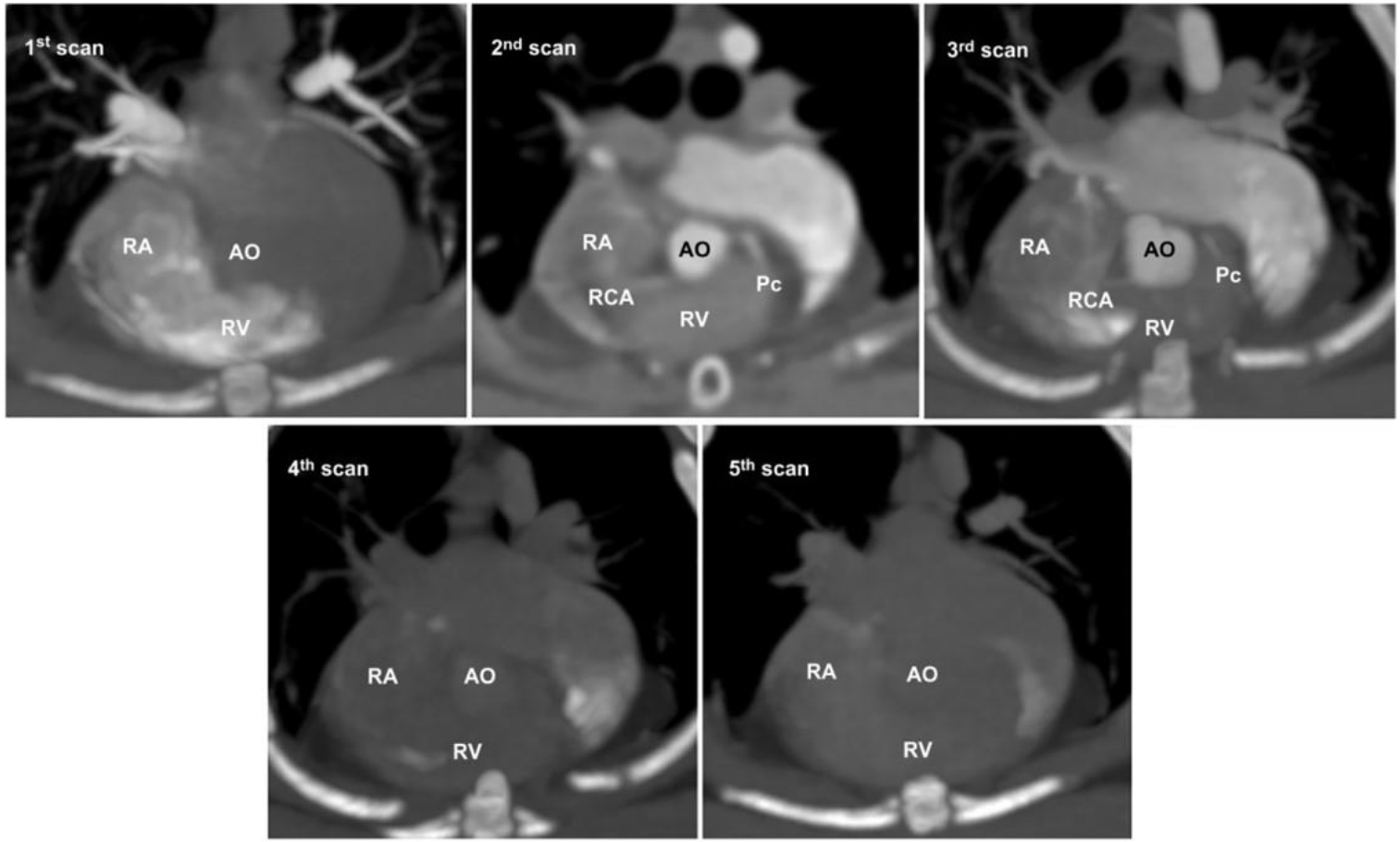

Figure 10. Five representative sequential non-electrocardiography (ECG)-gated multidetector computed tomographic images. In non-ECG-gated

images, the first image shows no contrast enhancement in the left heart. The second and third images allow visualization of the left and right main coronary stems at the origin but are non-diagnostic in terms of evaluating the detailed course of the coronary arteries owing to severe cardiac motion and blurring. The fourth and fifth images show poor opacification owing to the wash-out of the contrast medium. AO: aorta; Pc: paraconal interventricular branch; RA: right atrium; RCA: right coronary artery; RV: right ventricle.

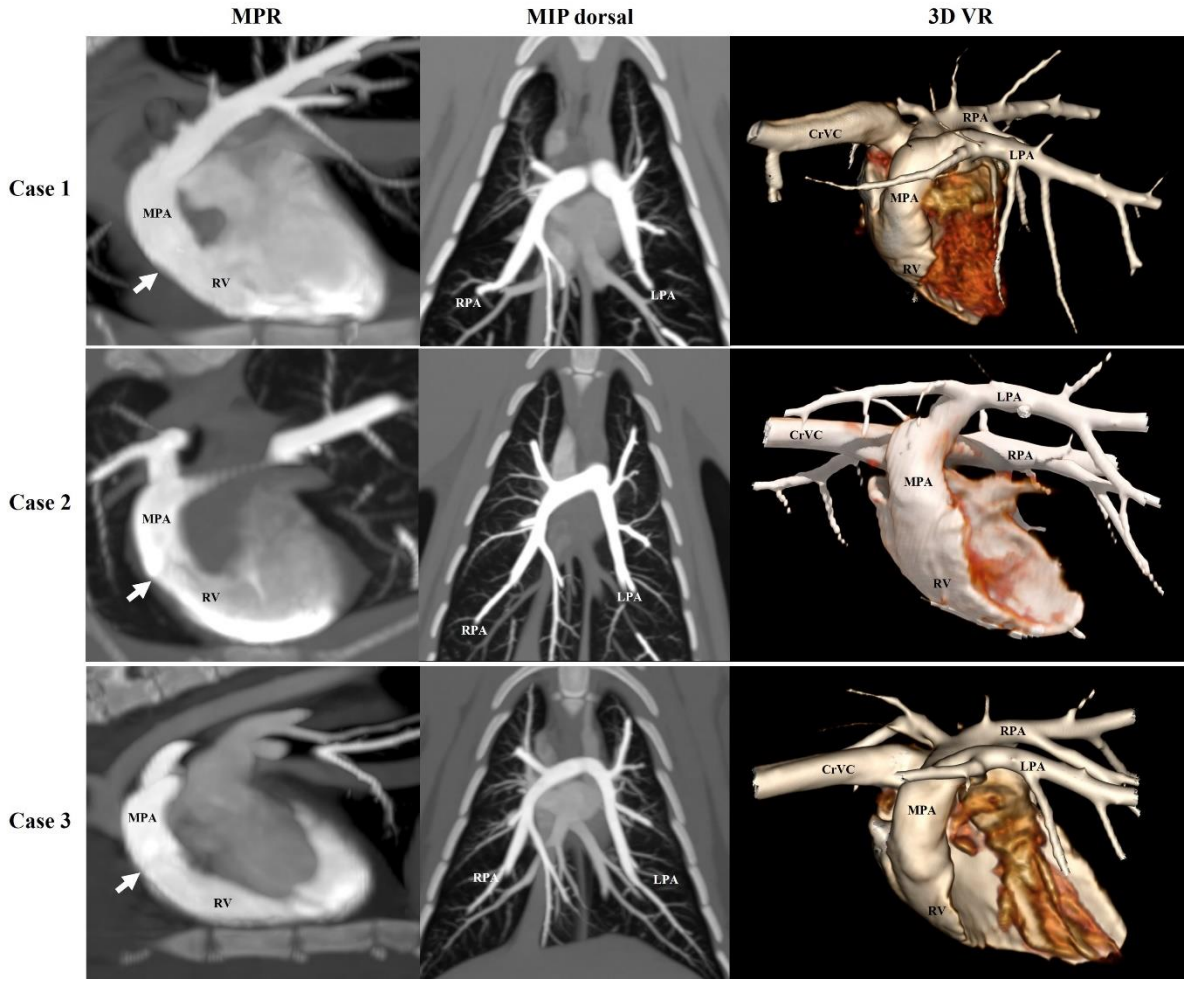
MPR
MIP dorsal
3D VR
Case 1
Case 2
Case 3
MPA
RV
RPA
LPA
CrVC

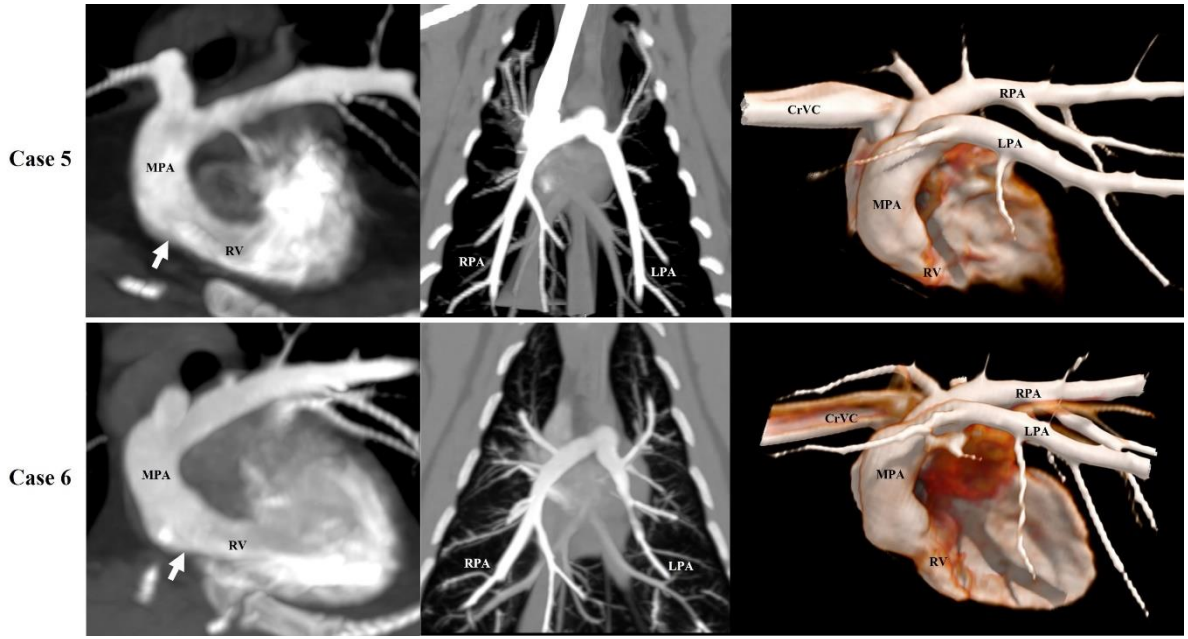

Figure 11. In the first scan of non-electrocardiography (ECG)-gated computed tomography in cats, multiplanar reconstruction (MPR), maximum intensity projection (MIP) dorsal, and three-dimensional (3D) volume rendered (VR) images were obtained. MPR images depict the right ventricular outflow tract (RVOT) and pulmonic valve (indicated by arrows). Additionally, MIP dorsal and 3D VR images illustrate the pulmonary arteries (PAs)and cranial vena cava (CrVC). In the non-ECG-gated scan method, the first scan images demonstrate excellent opacification in the CrVC, RVOT, and PAs. LPA: left pulmonary artery; MPA: main pulmonary artery; RPA: right pulmonary artery; RV: right ventricle.

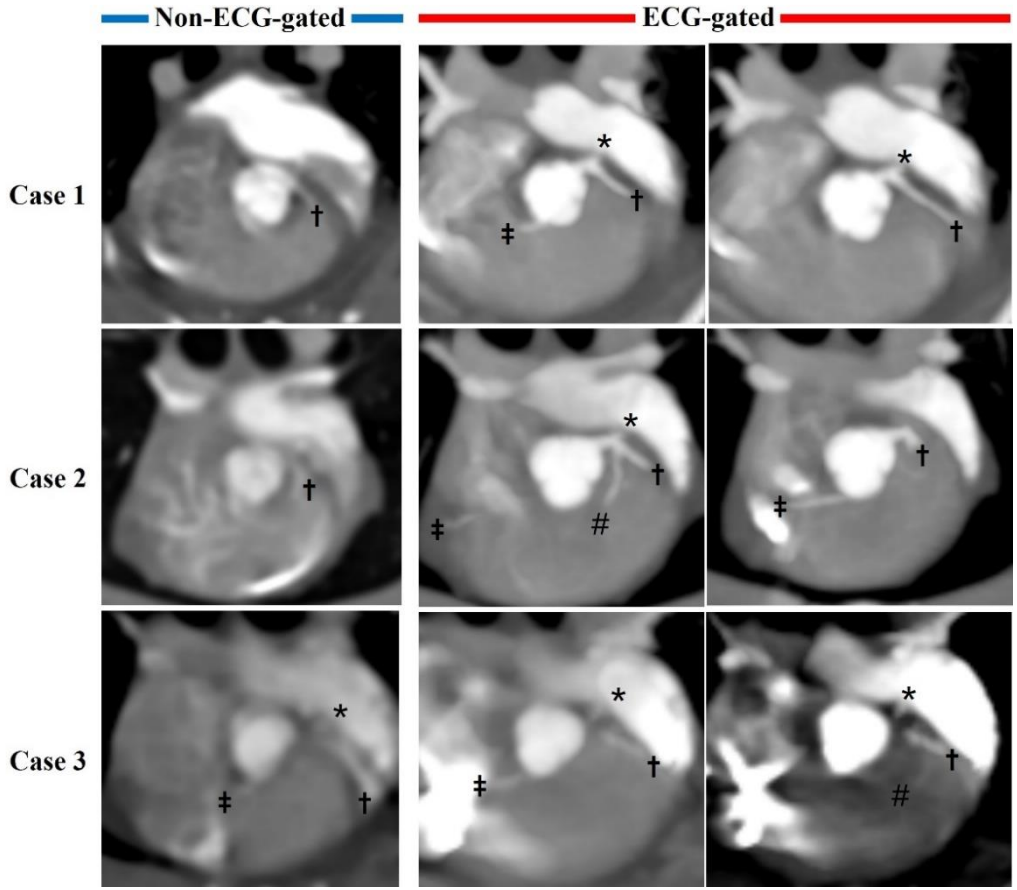
Non-ECG-gated
ECG-gated
Case 1
Case 2
Case 3

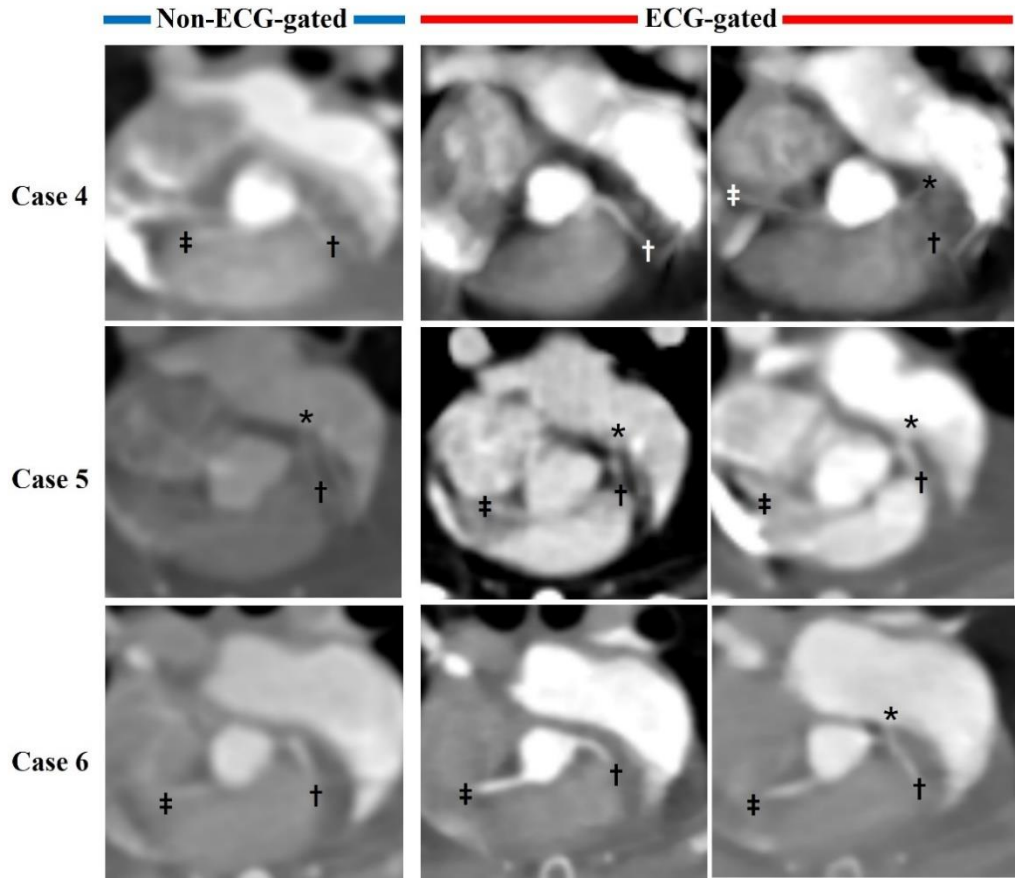

Figure 12. Maximal intensity projection (MIP) transverse images comparing the visualization of coronary arteries in the second scan of non-

electrocardiography (ECG)-gated and the optimal R-R interval of ECG-gated computed tomography in six cats. All six cats demonstrated clear visualization of their coronary arteries in ECG-gated images, compared to non-ECG-gated images. ⋆: circumflex; †: paraconal interventricular; ‡: right coronary artery; #: septal.

Table 6. Comparative evaluation of diagnostic quality based on the imaging of the main coronary artery (CA) branches using non-electrocardiography (ECG)- and ECG-gated 160-multislice computed tomography in cats

Case	Cx		Pc		S		Right CA	
	Non-ECG	ECG	Non-ECG	ECG	Non-ECG	ECG	Non-ECG	ECG
1	0	3	1	3	Absent	Absent	0	3
2	0	3	1	3	0	3	0	3
3	1	3	1	3	0	2	1	3
4	0	2	1	3	Absent	Absent	1	2
5	0	2	0	2	Absent	Absent	0	2
6	0	2	2	3	Absent	Absent	1	3

Grading system: 0: poor; 1: mild; 2: good; 3: excellent

Table 7. P-values for between-group comparisons of each coronary artery (CA) branch[a] in cats

CA branch	R[b] vs. Non-ECG	R vs. ECG	Non-ECG vs. ECG	Total
Cx	1.00	.008	.008	<.001
Pc	.060	.008	.026	0
S				
RCA	.727	.008	.008	0

CA, coronary artery; Cx, circumflex; ECG, electrocardiography; Pc, paraconal; R, reference group; RCA, right coronary artery; S, septal.
[a]P values for between-group comparisons were adjusted using Bonferroni correction.
[b]A virtual reference group using cases with non-cardiac computed tomographic images was set up. The imaging quality grade of the reference group was set at 0 for among-group comparisons.
The S branch was identified in only two cats, which limited the ability to perform statistical analysis.

2.3.3 Coronary dominance

Four cats exhibited left dominance and two exhibited right dominance (Table 8).

2.3.4 LCA branching types

CA branching types were characterized as type II in four cats, type I in one cat, and type III in one cat (Table 8). In the type III case, the Pc exhibited severe tortuosity, with two additional intermediate efferent branches originating from the proximal Pc branch, which were arbitrarily termed intermediate interventricularis paraconalis branches (Figure 13).

Table 8. Results of optimal R-R reconstruction intervals for visualizing the coronary arteries, as well as the coronary dominance and branching types of the left coronary artery (LCA) in electrocardiography (ECG)-gated computed tomographic images in six cats

Case No.	R-R interval	Coronary dominance	Branching types of the LCA
1	90%	Left	Type II
2	70%	Left	Type III
3	90%	Left	Type I
4	70%	Right	Type II
5	80%	Left	Type II
6	90%	Right	Type II

Type I: a double-branched left main coronary artery (LMCA) that gives rise to the circumflex (Cx) and interventricular paraconal (Pc) branches, which further branches off and gives rise to the septal (S) branch. Type II: a double-branched LMCA that gives rise to the Cx and Pc branches without an S branch. Type III: a triple-branched LMCA that gives rise to the Cx, Pc, and S branches.

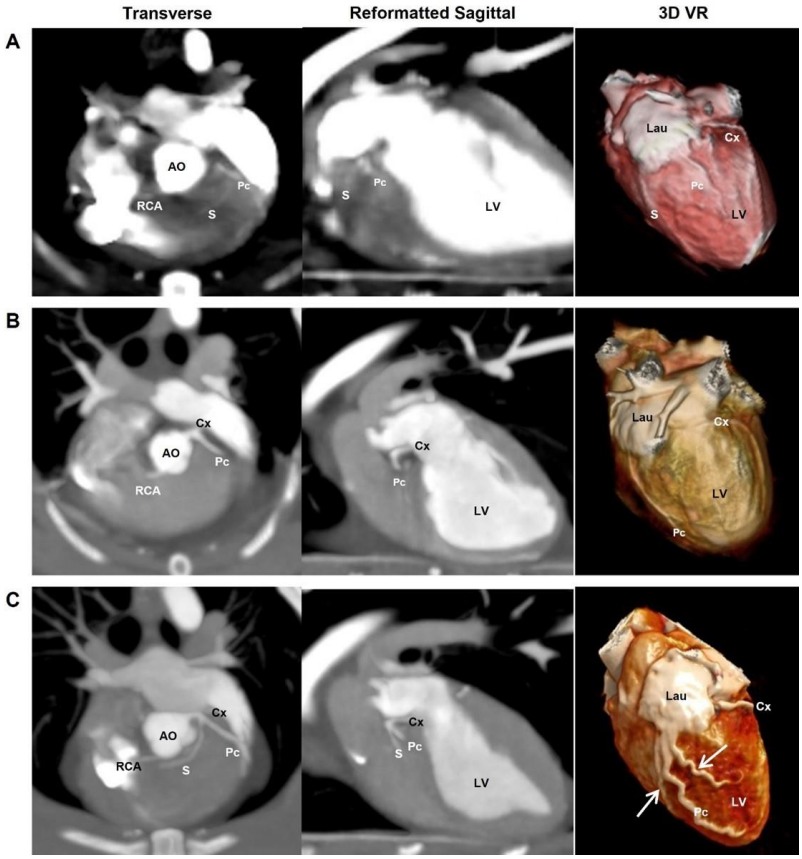

Figure 13. Two-dimensional transverse views, reformatted sagittal views and three-dimensional (3D) volume rendered (VR) images showing the three left coronary branching types in electrocardiography (ECG)-gated computed tomography. Type I (A) is characterized by a short left main coronary artery (LMCA) giving rise to the circumflex (Cx) branch and paraconal interventricular (Pc) branch, which branches off to the septal (S) branch. Type II (B) is characterized by a short LMCA giving rise to the Cx and Pc branches without an S branch. Type III (C) is characterized by a short LMCA giving rise to the Cx, Pc, and S branches. Panel (C) also illustrates severe tortuosity of the Pc branches and two additional intermediate efferent branches (arrows) from the proximal Pc branch. AO: aorta; Lau: left auricle; LV: left ventricle; RCA: right coronary artery.

2.3.5 Segmentation of the CAs

Left and right CA branches were further classified by adapting a previously described segmental coding system, whereby an arterial portion located between two reference points was considered an angiographic segment (Figure 9) (Auriemma *et al.*, 2018). The LCA originated from the left sinus of Valsalva in all cats. When the LMCA was present, it was classified as a single distinct segment before branching off, as classified above. The Cx and Pc were divided into three segments, as was the RCA (a total of 10 angiographic segments).

The three Cx segments were termed Cx1 (cranial segment), Cx2 (lateral segment), and Cx3 (caudal segment). The cranial segment ran caudally and ventrally to the left auricle and continued caudolaterally along the lateral surface of the left ventricular myocardium. The lateral segment ran perpendicular to the scanning plane into the coronary groove, laterally to the left atrioventricular junction, and ventral to the left circumflex vein. The caudal segment ran caudomedially to the left atrium, parallel to the scanning plane and along the caudodorsal surface of the left ventricle, and continued to run in the subsinosus interventricular groove, ending as the subsinosus interventricular branch. The Pc was classified into three segments: dorsal (Pc1), medium (Pc2), and apical (Pc3). The dorsal segment ran along the mid-dorsal aspect of the heart, caudoventrolaterally to the left, just caudal to the main pulmonary artery, ventromedially to the left auricle, and almost parallel to the scanning plane. The medium segment continued to run caudally along the mid-surface of the heart and within the Pc interventricular groove before ending as Pc3 along the ventral portion of the heart (apical portion). The S branch, which was observed only in two cats, ran laterally to the aortic bulb towards the interventricular septum (S1) and turned perpendicular to the scanning plane just ventral to the aortic bulb supplying the mid-

caudal aspect of the interventricular septum (S2).

The RCA originated from the right sinus of Valsalva and was classified into three segments: RCA1, RCA2, and RCA3. The first segment ran ventrally in the coronary groove, between the main pulmonic trunk and right atrium, almost parallel to the scanning plane. The second segment turned perpendicular to the scanning plane ventrolateral to the right atrium, into the right atrioventricular groove. The third segment ran caudodorsally, almost perpendicular to the scanning plane, and continued into the right atrioventricular groove on the diaphragmatic surface of the heart.

2.3.6 Diameter and length of the LCA and RCA

The diameters and lengths of the LCA and RCA in all cats are listed in Table 9. The mean ± SD of the major coronary branches, 95% CIs, and P-values of the analyses for all major CA branches, BW, sex, and VHS are also provided (Table 10, Figure 14). All datasets were normally distributed. For all CA branches, the length and diameter exhibited no significant correlations with BW or sex ($P > 0.05$) (Table 10, Figure 14). This study showed a significant negative correlation between VHS and LMCA, as well as a positive correlation between VHS and RCA ($P < 0.05$) (Table 10, Figure 14).

Table 9. Diameter and length of major coronary arterial branches

Case No.	Diameter (mm)					Length (mm)					
	LMCA	Pc	Cx	S	RCA	LMCA	Pc	Cx	S	Total LCA	RCA
1	1.7	1.4	1.5		1.2	4.1	45.1	38.7		87.9	31.0
2	1.7	1.3	1.3	1.2	1.2	4.8	46.9	34.2	21.8	107.7	24.0
3	1.2	1.2	1.5	1.1	1.3	4.2	39.7	37.9	22.8	104.6	33.6
4	1.2	1.5	1.2		1.1	4.4	50.3	25.3		80.0	36.7
5	1.3	1.4	1.3		1.5	4.3	32.4	35.2		71.9	20.7
6	1.4	1.3	1.2		1.5	3.9	34.5	21.6		60.0	46.0

Cx, circumflex; LCA, left coronary artery; LMCA, left main coronary artery; Pc, paraconal interventricular; RCA, right coronary artery; S, septal.

Table 10. Correlation of body weight (BW) and vertebral heart score (VHS) with diameter and length of the left and right coronary arteries

		Mean ± SD	BW		VHS	
			95% CI	P-values	95% CI	P-values
LMCA	Diameter	1.42 ± 0.23	-0.3836–0.2144	0.4762	-0.5165–0.3379	0.5929
	Length	4.28 ± 0.31	-0.4536–0.3905	0.8457	-0.5909– -0.2102	0.0043
Pc	Diameter	1.35 ± 0.1	-0.1217–0.1634	0.7054	-0.2218–0.1759	0.7646
	Length	41.48 ± 7.14	-11.97–1.576	0.1002	-16.68–7.809	0.3715
Cx	Diameter	1.33 ± 0.14	-0.2197–0.1444	0.5967	-0.2757–0.2476	0.8888
	Length	32.15 ± 7.04	-9.760–9.758	0.9997	-16.55–7.002	0.3232
Total LCA	Length	94.5 ± 17.08	-31.68–12.38	0.2909	-43.84–10.29	0.1604
RCA	Diameter	1.3 ± 0.17	-0.04412–0.2819	0.1128	-0.1777–0.3920	0.3552
	Length	32 ± 9.09	-15.24–7.696	0.4128	1.374–19.93	0.0333

CI, confidence interval; Cx, circumflex; LCA, left coronary artery; LMCA, left main coronary artery; Pc, paraconal interventricular; RCA, right coronary artery; SD, standard deviation.

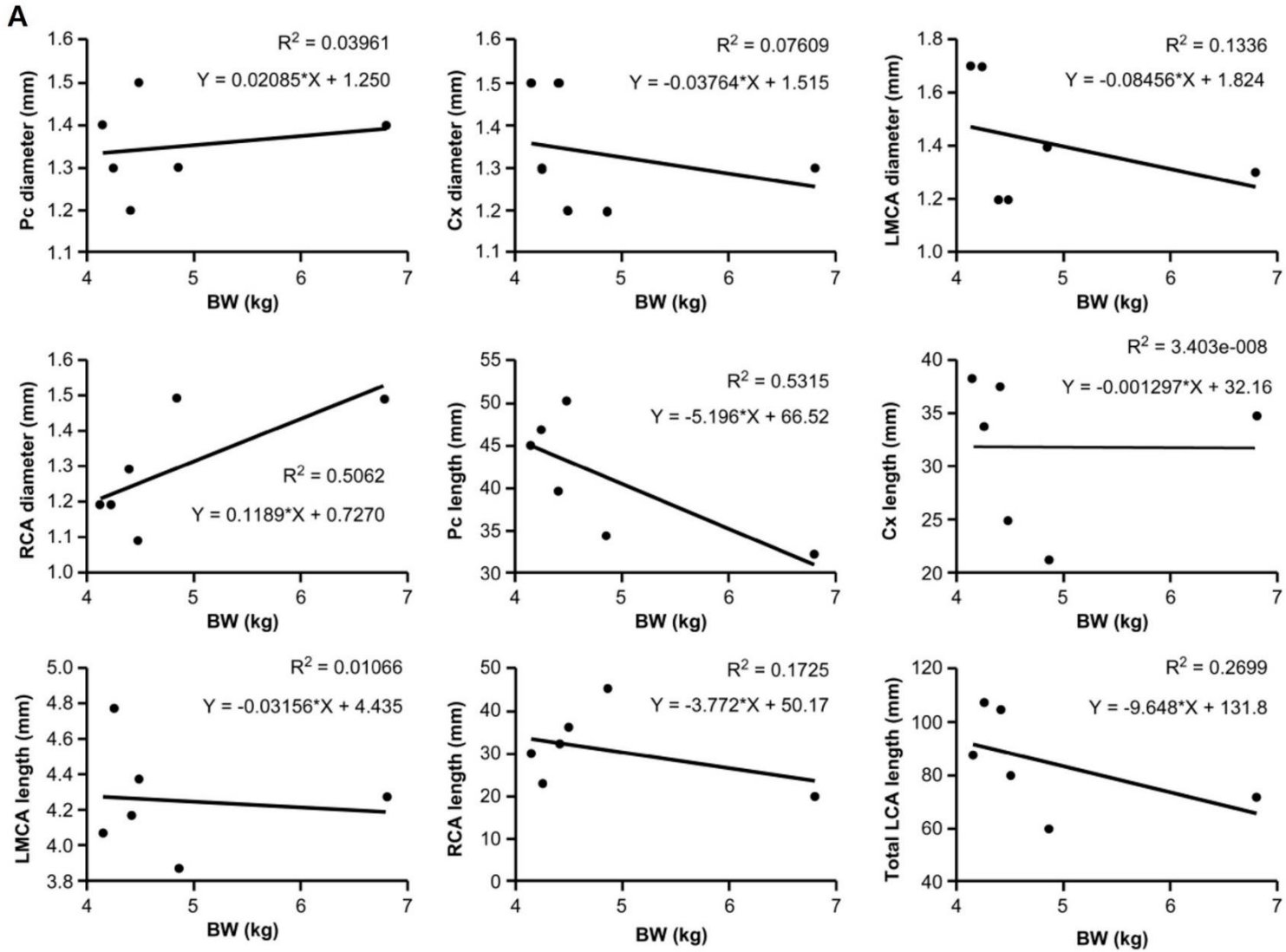
A
Pc diameter (mm)
BW (kg)
R2 = 0.03961
Y = 0.02085*X + 1.250
Cx diameter (mm)
R2 = 0.07609
Y = -0.03764*X + 1.515
LMCA diameter (mm)
R2 = 0.1336
Y = -0.08456*X + 1.824
RCA diameter (mm)
R2 = 0.5062
Y = 0.1189*X + 0.7270
Pc length (mm)
R2 = 0.5315
Y = -5.196*X + 66.52
Cx length (mm)
R2 = 3.403e-008
Y = -0.001297*X + 32.16
LMCA length (mm)
R2 = 0.01066
Y = -0.03156*X + 4.435
RCA length (mm)
R2 = 0.1725
Y = -3.772*X + 50.17
Total LCA length (mm)
R2 = 0.2699
Y = -9.648*X + 131.8

B

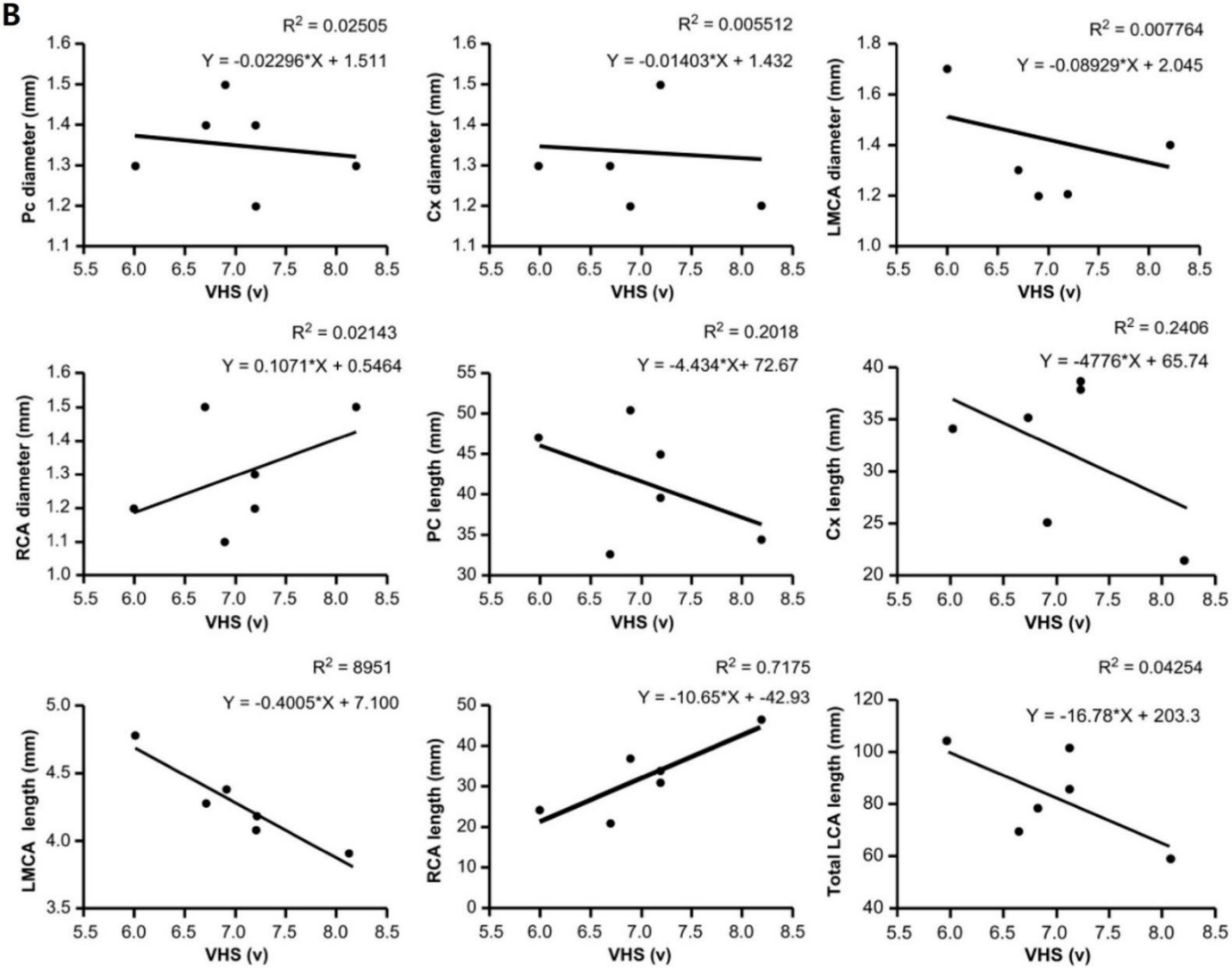
R2 = 0.02505
Y = -0.02296*X + 1.511
Pc diameter (mm)
VHS (v)
R2 = 0.005512
Y = -0.01403*X + 1.432
Cx diameter (mm)
VHS (v)
R2 = 0.007764
Y = -0.08929*X + 2.045
LMCA diameter (mm)
VHS (v)
R2 = 0.02143
Y = 0.1071*X + 0.5464
RCA diameter (mm)
VHS (v)
R2 = 0.2018
Y = -4.434*X+ 72.67
PC length (mm)
VHS (v)
R2 = 0.2406
Y = -4776*X + 65.74
Cx length (mm)
VHS (v)
R2 = 8951
Y = -0.4005*X + 7.100
LMCA length (mm)
VHS (v)
R2 = 0.7175
Y = -10.65*X + -42.93
RCA length (mm)
VHS (v)
R2 = 0.04254
Y = -16.78*X + 203.3
Total LCA length (mm)
VHS (v)

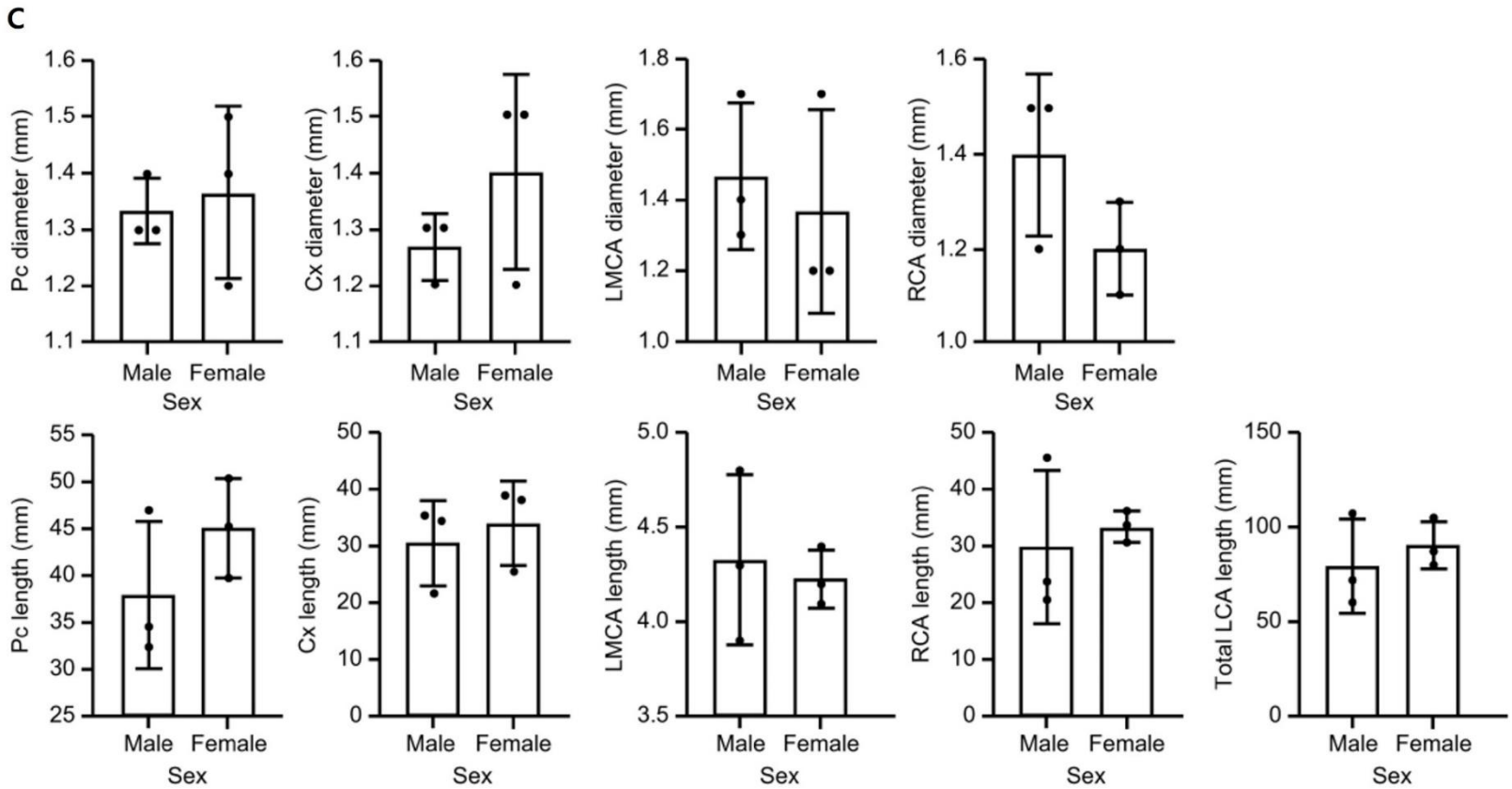

Figure 14. Scatter plots of the association between (A) body weight (BW) and major coronary branches, and (B) vertebral heart score (VHS) and major coronary branches in domestic short-haired cats. (C) Box plots showing the correlation between sex and major coronary branches in domestic short-haired cats. Cx: circumflex; LCA: left coronary artery; LMCA: left main coronary artery; Pc: paraconal interventricular; RCA: right coronary artery.

2.4 Discussion

The current findings demonstrate that ECG-gated, 160-slice cardiac CT angiography is an effective method for obtaining diagnostic images for the evaluation of feline CAs, without the need for heart rate modulation or beta-blocker administration. The scanning protocol used in this study is the first to establish the delay time for ECG-gated scans based on non-ECG-gated images, without bolus tracking or a test bolus, enabling successful acquisition of ECG-gated scans. Furthermore, the first-scan non-ECG-gated scan images provided clear visualization of the CrVC, RVOT, and PAs. It is believed that this modified scanning method is expected to provide clinically valuable information in patients with various cardiovascular diseases, including PS, persistent left CrVC, and CrVC syndrome with secondary chylothorax (Heaney *et al.*, 2004; Letendre *et al.*, 2015; Schrope DP, 2008). The modified method allows for the simultaneous evaluation of bilateral circulation of the heart, enabling comprehensive cardiac assessment and guiding appropriate diagnosis and treatment planning (drees *et al*., 2014). While the primary aim of this modified scanning method was to directly compare non-ECG and ECG-gated images in the same patient, our findings also suggest that selecting the delay time, reducing radiation exposure, and expanding the fourth or fifth non-ECG scan range may be advantageous for patients requiring abdominal or whole-body scans beyond the heart. Therefore, the new (modified) cardiac CT protocol in this study holds clinical utility in veterinary medicine.

The detailed course of CAs was difficult to evaluate on non-ECG MDCT scans due to poor opacification and substantial motion artifacts, although the bilateral coronary ostium and proximal CA segments could be visualized on the second and third scans. These findings indicate that non-ECG MDCT scans can provide the minute information required to evaluate congenital single CA diseases, similar to findings observed in previous canine studies (Visser *et al.*, 2013; Gunther-Harrington *et al.*, 2019; Stieger-Vanegas *et al.*, 2019).

This study describes feline LCA branching types using cardiac MDCT. Type II, which does not involve S branches, was the most predominant type, occurring in four of the six cats. This type has not been reported in dogs to date (Noestelthaller *et al.*, 2007; Drees *et al.*, 2011b; Auriemma *et al.*, 2018). In a previous morphological study of CAs in 48 cats, type I (49%) was the most predominant, followed by type II (26%). Here, we observed both left (four cats) and right (two cats) coronary dominance. These results highlight the morphological variability of feline CAs, consistent with a previous report (Scansen, 2017). In one cat with type III branching (i.e., three main CA branches simultaneously extending from the LMCA), severe tortuosity of the Pc and two additional efferent branches, a pattern that has not been reported in previous studies, were observed. Studies on humans have reported that coronary tortuosity may lead to alterations in coronary flow, resulting in a reduction in coronary perfusion pressure distal to the tortuous coronary arterial segment, subsequently leading to myocardial ischemia (Gaibazzi *et al.*, 2011; Estrada *et al.*, 2017; Khosravani-Rudpishi *et al.*, 2018). Moreover, coronary tortuosity is positively associated with arterial hypertension and the female sex (Estrada *et al.*, 2017). The cat with coronary tortuosity herein was a 3.6-year-old intact male that exhibited normal clinical findings on the basic health check-up. Therefore, this cat should be monitored for myocardial disease with consistent cardiac assessments. Further research is warranted to clarify the clinical implications of feline coronary tortuosity.

In the current study, the diameters of the LCA and RCA were considered short relative to their length. The diameters of the LMCA and RCA were 1.42 ± 0.23 mm and 1.30 ± 0.17 mm, respectively, in contrast to a previous report indicating that the diameter of the RCA was slightly larger (Barszcz *et al.*, 2017). Three cats also had a slightly larger RCA than LCA at 0.1–0.2 mm, in contrast to the previous finding indicating that the value for the LCA ostium was greater than that for the RCA (Barszcz *et al.*, 2017). Considering the possibility of subtle measurement differences on CT images and the limited sample size in this study, these findings suggest the

possibility that the LCA and RCA diameters may be similar. A canine study reported positive correlations between the CA and BW, including the LCA and RCA diameter, as well as the length of the Cx and Pc branches (Auriemma *et al.*, 2018). However, no significant correlation between the diameter or length of CAs and BW was observed herein. This may have been due to the small sample size and small weight variation (4.82 ± 1.00 kg) of the cats in our study when compared with those in previous canine studies. The heaviest cat (Case 5) in our study had a similar CA diameter but shorter CA length than those of other cats, indicating that BW may not affect CA length or diameter.

Coronary dominance of the heart refers to whether the LCA or RCA perfuses the majority of the myocardial tissue. Variable methods have been adopted to determine this parameter (de Oliveira *et al.*, 2011; Auriemma *et al.*, 2018). For a comparison with canine coronary MDCT results, we investigated which CA supplied the subsinosal interventricular branch and which CA extended beyond the crux of the heart, as reported previously (Auriemma *et al.*, 2018). Other parameters, including the origin or layout of the arteries at the heart apex, as well as the relative lengths and numbers of LCA/RCA branches, appeared similar between the present and previous studies. In contrast to the left-dominant coronary circulation in dogs, our findings indicate that cats exhibit variable dominance, despite the small sample size (de Oliveira *et al.*, 2011; Scansen, 2017; Auriemma *et al.*, 2018). Herein, the Cx branch of four left-dominant cats and the RCA branch of two right-dominant cats supplied the subsinosal interventricular branch with the extension beyond the crux cordis.

In the current study, the cat diagnosed with HCM phenotype during a basic health check-up exhibited a positive result on pro-BNP tests, cardiomegaly (VHS 8.2 v) on thoracic radiography, and regional thickening of the interventricular septum (0.66 cm) in the right parasternal short-axis view on ECG. As there were no abnormalities in the left atrium-to-aorta ratio (1.56; reference range, 0.88–1.70), diastolic function, systolic anterior motion of the mitral valve, or

other examinations, the cat was able to undergo a cardiac CT scan. The cat with HCM phenotype exhibited a type II LCA branching pattern, which was the most predominant in our study, as well as right coronary dominance and marked right coronary length. This may have partly underpinned the positive correlation between VHS and RCA herein. HCM is a primary myocardial disorder, indicating that myocardial abnormalities are due to a defect most often within the sarcomeres (i.e., individual contractile elements within the heart) of the cardiomyocytes, and are not secondary to other causes, such as hyperthyroidism, systemic hypertension, aortic stenosis, or acromegaly (Côté *et al.*, 2011). We hypothesize that these contractile myocardial defects influence the contractile wall of the left heart with a diminished left coronary flow, resulting in compensatory concentric hypertrophy. The role of CA perfusion in cats with cardiomyopathy still requires further investigation in feline patients using MDCT, similar to studies conducted in humans (Pelliccia F *et al*., 2022).

This study has some limitations, including a small sample size that comprised only five healthy cats and one with HCM. Further, there was no confirmation based on gross findings or biopsy in this study. Despite these limitations, this prospective study of feline CAs using a new (modified) cardiac CT protocol holds clinical significance for veterinary medicine. In human medicine, the assessment of CA morphology is performed not only to diagnose certain diseases but also before open and endovascular or cardiovascular procedures (Barszcz *et al.*, 2017). Furthermore, in veterinary medicine, anatomical studies of the aorta and CAs are conducted in animals and used as experimental models prior to human clinical trials (Barszcz *et al.*, 2017). Although the surgical interventions mentioned above have not been widely performed in veterinary medicine, research in this field and increased awareness of pet owners may warrant such procedures. Detailed morphological knowledge of feline coronary vessels will enable novel diagnostic and therapeutic methods, as well as facilitate the implementation of endovascular procedures that are commonly used in humans in veterinary medicine.

In conclusion, the new (modified) cardiac CT scan protocol used in this study, which involved non-ECG-gated scans followed by ECG-gated scans, allowed for sufficient visualization of the bilateral cardiac circulation and CAs without the need for bolus tracking. This modified protocol provided valuable information regarding feline CAs and indicated the potential existence of various normal CA patterns in cats. However, further research involving a larger sample size of cats with various cardiovascular diseases is necessary to establish the clinical feasibility of cardiac CT in evaluating the feline cardiovascular system, including the CAs.

Chapter 3. Evaluation of the Pulmonary Vein Ostia in ECG-gated Images of a Modified Cardiac CT Protocol in Cats

3.1 Introduction

Pulmonary veins (PVs) and their ostia, which are important sources of ectopic atrial activity, have been implicated in chronic and paroxysmal atrial fibrillation (Kim *et al.*, 2005; Cronin *et al.*, 2007; Manghat *et al.*, 2012; Lye *et al.*, 2019). Radiofrequency ablation of the PV is performed for patients with atrial fibrillation to disconnect the PV electrically from the left atrium (LA) in humans; thus, detailed anatomical information about the PV is important for catheter size selection during the ablation procedure (Hamabe *et al.*, 2003; Cronin *et al.*, 2007; Manghat *et al.*, 2012; Lye *et al.*, 2019). The PV also constitutes an essential aspect of thoracic interventions such as lung transplantation and pneumonectomy; moreover, PV congestion is a clinically important indicator of elevated PV pressure, a cause of pulmonary edema (Merveille *et al.*, 2015; Hassani & Saremi, 2017). Therefore, detailed anatomical knowledge of the PV is important clinically in both human and veterinary medicine.

Technological advancement with ECG-gating method have enabled detailed visualization of the anatomical features of cardiovascular structures using MDCT (Cronin *et al.*, 2007; Manghat *et al.*, 2012). Several studies in humans have reported detailed anatomical information on the PV and ostium and the use of ECG-gated MDCT to evaluate the dimensional variations of the PV or ostium according to the cardiac cycle (Choi *et al.*, 2005; Cronin *et al.*, 2007; Manghat *et al.*, 2012; Ratajczak *et al.*, 2016; Hassani & Saremi, 2017). These studies have demonstrated significant dimensional differences in the PV and ostia between the ventricular end-systole and ventricular end-diastole, which apparently become less significant further from the LA (Choi *et*

al., 2005; Manghat *et al.*, 2012). Moreover, patients with chronic atrial fibrillation and LA enlargement may have larger PVs and ostia than those with paroxysmal atrial fibrillation and a normal-sized atrium (Kim *et al.*, 2005; Cronin *et al.*, 2007). These results suggest the clinical significance of ECG-gated MDCT in evaluating the PV and ostium in human medicine.

However, there is still a significant need for research in veterinary medicine to evaluate the PV or ostium using MDCT. Most veterinary studies on pulmonary vessels using MDCT have focused primarily on the PAs, and studies related to the PVs have reported only on PV drainage patterns and the number of PV ostia in dogs and cats (Drees *et al.*, 2011a; Habing *et al.*, 2011; Brewer *et al.*, 2012; Reid *et al.*, 2012; Lee-Fowler *et al.*, 2017; Panopoulos *et al.*, 2019). Therefore, it is necessary to investigate the diametric variation in the PV or ostium during the cardiac cycle using ECG-gated MDCT in veterinary medicine as well. Additionally, although the PV to PA ratio has been evaluated as a predictive factor for congestive heart failure using echocardiography, evaluation of the PV or ostium using MDCT may be clinically useful in the future, considering the limitations of echocardiographic examination arising from its considerable dependence on the operator's scan techniques and/or patient respiration.

Therefore, the purpose of this study was to investigate the variations in the diameter of the PV ostium during the cardiac cycle in cats using ECG-gated images in Chapter 2. Furthermore, the relationship between the size of the heart or LA and the diameter of the PV ostium was investigated. The hypothesis was that changes in the diameter of the PV ostium throughout the cardiac cycle would be detectable in the ECG-gated images, and the study aimed to provide evidence supporting the advantages of utilizing exclusively ECG-gated images.

3.2 Materials and Methods

3.2.1 Animals

This study represents a retrospective analysis of a subset of the original prospective study (chapter 2). Data from five clinically normal cats and one cat with HCM that underwent ECG-gated MDCT were analyzed retrospectively. The study design and care, as well as animal maintenance, followed protocols approved by the Institutional Animal Care and Use Committee of Seoul National University in February 2022 (approval number: SNU-220113-4). Medical history and informed consent were obtained from the owners for all client-owned cats prior to all procedures. Six domestic short-haired cats with no clinical signs provided by the owners were included. Before MDCT examination, all cats underwent basic health tests, including physical examination, complete blood count, serum biochemistry, and electrolyte tests. Cardiac evaluation was performed using NT-proBNP testing, thoracic radiography, and transthoracic echocardiography (Aplio 500®, Canon Medical Systems). Two-dimensional, M-mode, and Doppler echocardiography was performed for all cats. The time interval between all basic health tests and MDCT examination for each cat was less than five days.

3.2.2 Anesthesia

An intravenous 24-G catheter was placed in the right cephalic vein for premedication and injection of the contrast agent during MDCT. General anesthesia was induced as follows: premedication with butorphanol (0.2 mg/kg intravenously; 1 mg/mL, Butophan®; Myungmoon Pharm Co., Ltd.), induction with propofol (6 mg/kg intravenously; 10 mg/mL, Provive® 1%, Myungmoon Pharm Co., Ltd.), and maintenance with isoflurane (Isotroy® 100, Troikaa Pharm Ltd.) in a gaseous mixture of 100% oxygen via an endotracheal tube. End-tidal carbon dioxide levels were maintained between 35–45 mmHg using a mechanical ventilator. During anesthesia,

the heart rate, oxygen saturation, and end-tidal carbon dioxide were monitored continuously using ECG, pulse oximetry and capnography. Data acquisition was initiated within 5–10 min after induction of anesthesia to ensure the stability of anesthetic conditions. For individual scans, apnea was induced by breath-holding at inspiration immediately before the scan. All cats were monitored until recovery from anesthesia.

3.2.3 ECG-gated cardiac CT

All MDCT examinations were performed using an 80-row, 160-multislice CT system (Aquilion Lightning®, Canon Medical Systems). During the examination, the patients were positioned in sternal recumbency on a CT table with the neck extended and the forelimbs placed caudally. ECG leads were attached to the paws; ECG data were recorded simultaneously during spiral MDCT examination. The scan protocol was as follows: voltage, 120 kVp; gantry speed, 0.5 s/rotation; slice collimation, 0.5 mm × 80; 150 mA; slice thickness, 0.5 mm; and pitch factor, 0.813. All patients underwent a non-ECG-gated scan, followed by a retrospective ECG-gated scan after a short interval (5 min) to allow washout of the contrast medium from the heart. All cats underwent a pre-contrast MDCT scan of the full thorax from the thoracic inlet to the most caudal border of the lungs before the post-contrast studies. For non-ECG-gated scans, the following were injected into the cephalic vein using a dual power injector (OptiVantage™ DH, Mallinckrodt) at a rate of 1.5 mL/s: a biphasic injection, a non-ionic contrast medium (300 mgI/mL, Omnipaque®; GE Healthcare) at 1.5 mL/kg, followed by a saline flush (0.9% NS®; Dai Han Pharm Co., Ltd.) at 1.5 mL/kg. After 8 s of contrast injection, five sequential scans were performed over the cardiac silhouette from the cranial to the caudal side at 5-s intervals. The delay time for retrospective ECG-gated scans was 14 s in all cats; this was determined based on non-ECG-gated sequential scan images without bolus tracking to reduce radiation exposure and anesthesia time. The contrast medium administration for ECG-gated MDCT was

conducted in the same manner as that for the non-ECG-gated scan. For data post-processing, images were reconstructed in multiple datasets, by increasing the temporal reconstruction window in 10% increments within the cardiac cycle, centered over the 0–90% R-R interval. All images were reviewed by three veterinary diagnostic imaging experts (Junyoung Kim, Kitae Kim, Dayoung Oh) on a dedicated viewing station using specialized software (Vitrea 7.12®, Vital Images), which depicted MIP, 3D VR, and multiplanar reconstructions to optimize visualization of the PV and ostium.

3.2.4 Evaluation of the PV ostium in cats

1) Number of PV ostia within the LA and classification of the PV drainage system just before opening into the PV ostium

The PV drainage system was classified according to a previous study (Panopoulos *et al.*, 2019): (a) separate, when the PVs drained independently into the LA; (b) short common trunk, when two or more PVs fused by forming a "short neck" just before opening into the LA; or (c) long common trunk, when two or more PVs fused by forming a "long neck" just before opening into the LA.

2) Variation in the PV ostial diameter during the cardiac cycle on ECG-gated MDCT

In 10 sets of phase reconstruction data, ranging from 0–90% in 10% increments of the R-R interval on the ECG in all cats, the diameter of each PV ostium entering the LA according to the cardiac cycle was measured and compared through the same cross-section at the MIP oblique transverse or coronal planes, by dropping a perpendicular to the long axis of the PV. The ostium is defined as the point of inflection between the PV and LA walls, and the ostial diameter was measured from PV wall to PV wall (Figure 15). Measurement of each PV ostial diameter according to the cardiac cycle was performed three times each by three veterinary diagnostic imaging experts, and the overall mean value of each of the three veterinary

diagnostic imaging experts' mean values was determined as the final value. The diameter of each PV ostium at ventricular end-systole (30–40% R-R interval) and ventricular end-diastole (0%, 70–90% R-R interval) was selected and compared among all cats. Furthermore, the reconstruction windows showing the maximal and minimal diameters of the ostia of all PV measured during the cardiac cycle were selected.

3) Correlation between the PV ostial diameter and sizes of the heart or LA

In all cats, the maximal or minimal values of the PV ostial diameters were compared with the VHS on thoracic radiography or LA to aorta (AO) ratio on echocardiography.

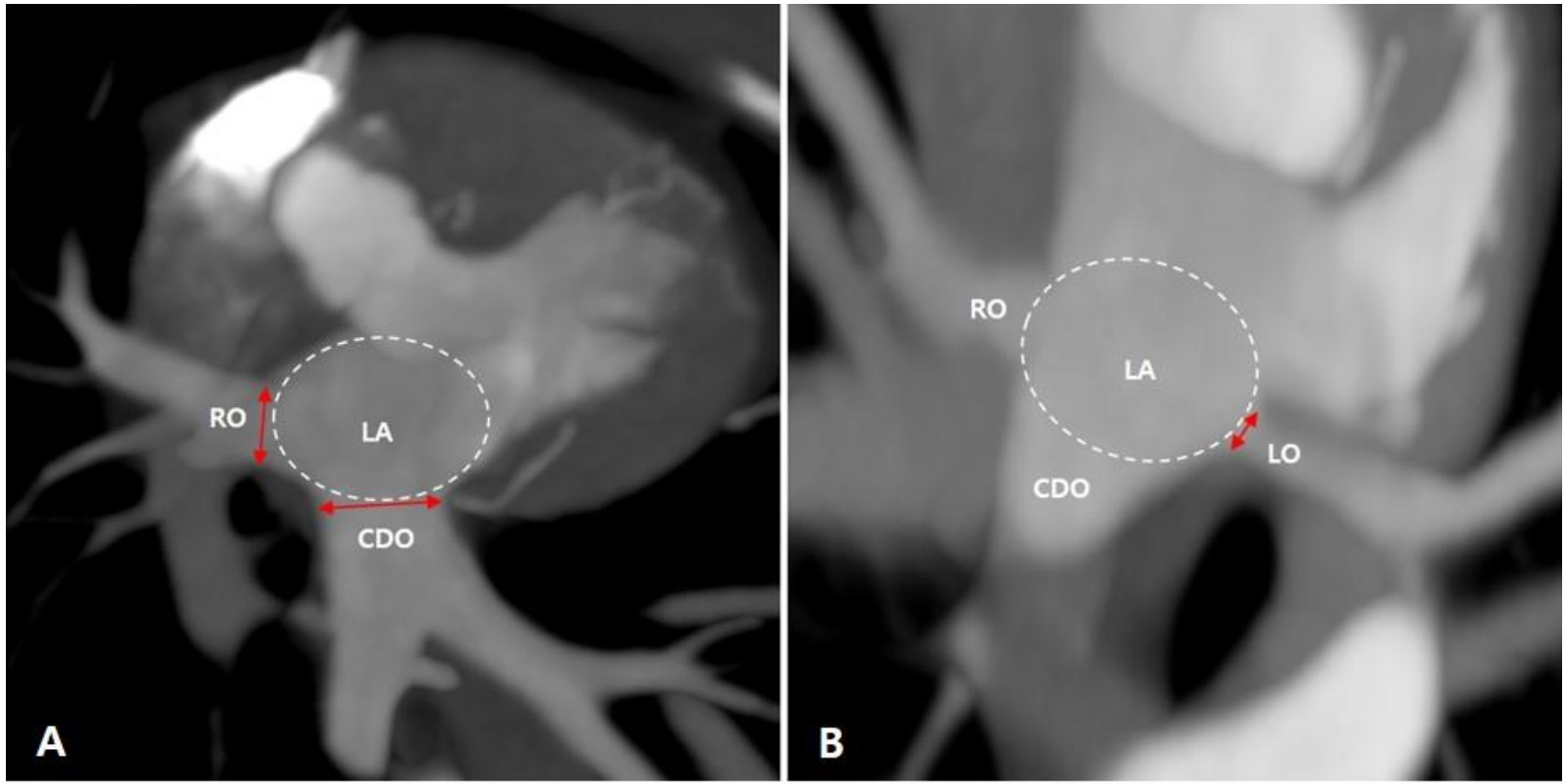

Figure 15. Measurement of the pulmonary vein (PV) ostial diameter. First, the maximum intensity projection of the oblique transverse or coronal planes for best visualization of each PV ostium were selected using multiplanar reconstruction, and then each PV ostial diameter during the cardiac cycle was measured and compared at the same cross-section. Each ostium is defined as the point of inflection between the PV wall and the left atrial (LA) wall, and the ostial diameter was measured from the PV wall to the PV wall. (A) indicates the measurement of the

diameter in the right cranial ostium (RO) and caudodorsal ostium (CDO), and (B) indicates the left cranial ostium (LO).

3.2.5 Statistical analyses

All data are expressed as means ± SDs. Statistical analyses were performed using SPSS 26.0 (IBM, Armonk, NY, USA). As the data were not normally distributed owing to the small sample size, we used non-parametric tests, except for the comparison of the PV ostial diameter between the end-systolic and end-diastolic phases. Spearman's rho test was used to identify the statistical correlations between age, BW, VHS or LA/AO ratio, and maximal or minimal diameter of each PV ostium. The Kruskal-Wallis test was used to compare all values with respect to sex. An independent t-test was used to compare the mean value of each PV ostium at the ventricular end-systolic and ventricular end-diastolic phases. A one-sample *t*-test was used to compare the statistically significant differences among the five clinically normal cats and one cat with HCM phenotype for the BW, VHS, LA/AO ratio, and maximal/minimal diameter of each PV ostium. A p-value <0.05 was considered statistically significant.

3.3 Results

Of the six domestic short-haired cats included in this study, three were spayed females and three were males (one intact, two neutered). The mean age was 4.85 ± 3.74 years, the mean BW was 4.82 ± 1.00 kg, the mean VHS was 7.03 ± 0.72 v, and the mean LA/AO was 1.27 ± 0.22 (Table 5). Of the six cats, five were normal in terms of all basic health tests, although one HCM phenotype cat (Case 6) showed regional thickening (0.66 cm) of the interventricular septum and a positive result in the NT-proBNP test (Table 5). This cat had a systemic blood pressure of 150 mmHg and a normal serum thyroid hormone concentration at 2.1 μg/dL (reference range, 0.6–3.9 μg/dL).

The new (modified) cardiac CT protocol utilized in this study allowed for the acquisition of ECG-gated CT images, which enabled the measurement of the ostial diameter of each PV as it enters the LA throughout the cardiac cycle in all cats. (Figure 15, 16). The total time from induction of anesthesia to the end of the MDCT examination ranged between 25–35 min, with an average of 30 min per animal. The heart rate during the MDCT scan ranged from 120–150 bpm in all cats. No complication associated with the anesthetic protocol was documented during the procedure. The PVs drained into the LA via three ostia [i.e., the right cranial ostium (RO), left cranial ostium (LO), and caudodorsal ostium (CDO)] which were identified in all cats (Figure 17) (Panopoulos *et al.*, 2019). The RO, draining from the PVs of the right cranial and middle lung lobes, formed a long common trunk before opening into the right cranial part of the LA. The LO, draining from the PVs of the cranial and caudal parts of the left cranial lung lobe, also formed a long common trunk before opening into the left cranial part of the LA. The CDO, draining from the PVs of the bilateral caudal and accessory lung lobes, formed a short common trunk before opening into the caudodorsal part of the LA. These findings were similar to those of a previous study (Panopoulos *et al.*, 2019).

As a result of PV diameter measurement using a specialized software, the average value of three veterinary diagnostic imaging experts showed consistent results. In this study, the CDO was found to be the largest and the LO the smallest, and all ostia showed dimensional variation during the cardiac cycle (Table 11). The maximal diameter was achieved at end-systole (30–40% R-R interval) except in two cases (50% R-R interval), and the minimal diameter was achieved at end-diastole (0%, 70–90% R-R interval) except in one case (50% R-R interval) (Table 11). In all six cats, the average diameter of each PV ostium according to the cardiac cycle was the maximum at the end-systole and minimum at the end-diastole (Figure 18). There was a significant difference in the mean diameter of each PV ostium between end-systole and end-diastole ($p<0.05$) (Table 12). There were no statistical correlations between the maximal or minimal diameter of all PV ostia and age, BW, sex, VHS, or LA/AO ratio ($p>0.05$). One cat with HCM phenotype showed a significant enlargement in the VHS and LA/AO ratio compared with the other five normal cats ($p<0.05$), but showed no significant differences in all PV ostial diameters between the two groups ($p>0.05$).

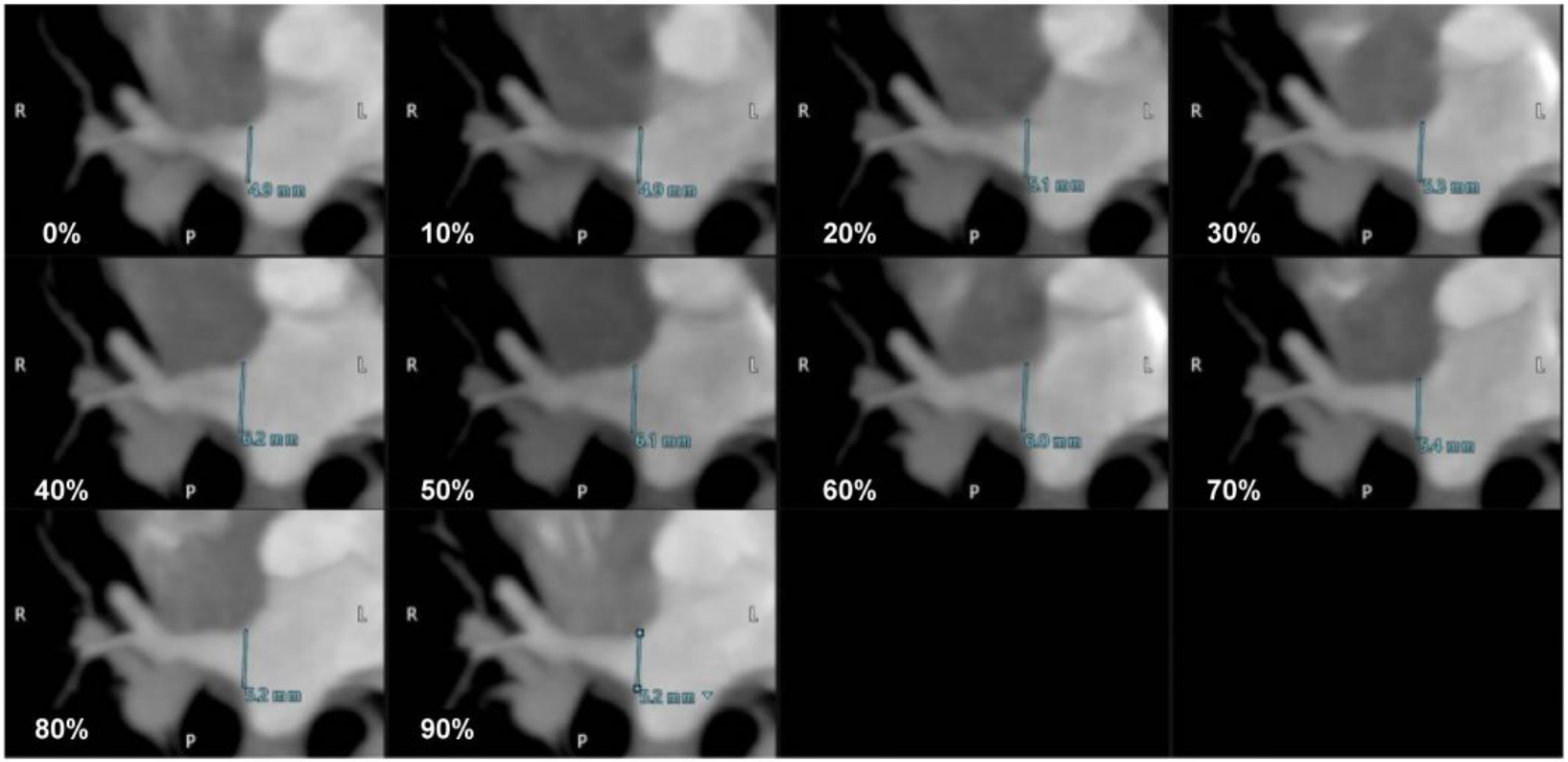

Figure 16. Maximum intensity projection oblique transverse images showing the dimensional variation of the right cranial ostium according to the cardiac cycle (0–90% R-R interval) in a cat.

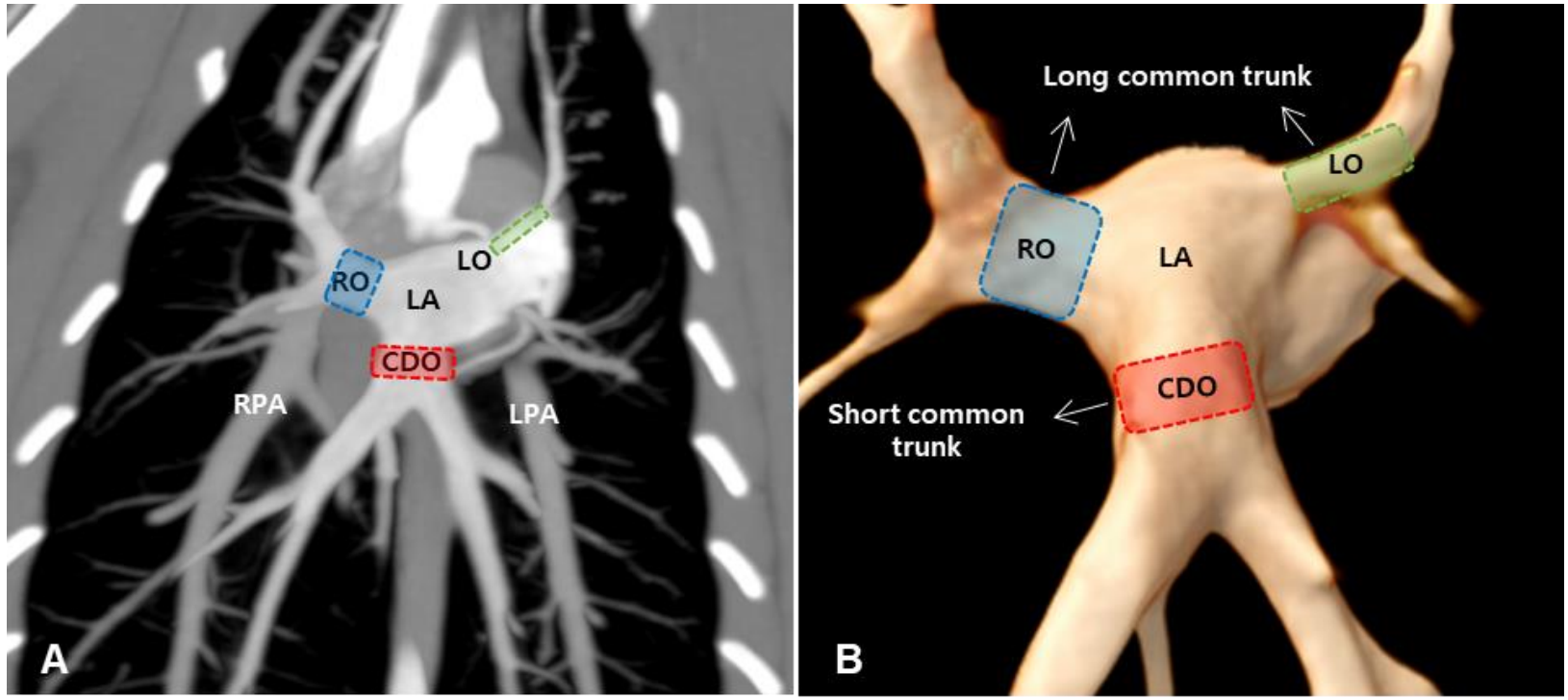

Figure 17. Maximum intensity projection (A) and three-dimensional volume-rendered images (B) showing the pulmonary vein's (PV) ostia entering the left atrium (LA) in cats. There were three PV ostia—the right cranial ostium (RO), left cranial ostium (LO), and caudodorsal ostium (CDO), in this study. RPA; right pulmonary artery, LPA; left pulmonary artery.

Table 11. The mean value of the three pulmonary vein ostial diameters according to the cardiac cycle in six cats.

RR interval	Case 1			Case 2			Case 3			Case 4			Case 5			Case 6		
	RO	CDO	LO	RO	CDO	LO	RO	CDO	LO	RO	CDO	LO	RO	CDO	LO	RO	CDO	LO
0%	4.2	7.4	1.8	4.9	7.4	1.7	4.5	7.2	2.0	4.8	7.1	1.9	4.8	7.1	2.0	5.2	7.3	2.4
10%	4.6	7.6	2.0	4.9	7.3	1.8	4.5	7.4	2.2	4.9	7.5	2.0	4.9	7.4	1.9	5.4	7.3	3.0
20%	4.7	7.8	2.4	5.1	7.4	2.0	4.5	7.6	2.2	5.3	7.8	2.2	5.4	7.4	2.3	5.8	8.2	2.9
30%	5.1	7.9	2.5	5.3	7.7	1.9	5.5	8.1	2.2	5.7	7.9	2.5	5.6	7.5	2.2	6.3	8.3	3.0
40%	4.9	8.4	2.2	6.2	7.7	2.1	5.4	8.0	2.3	6.8	7.7	2.6	6.1	8.3	2.5	6.4	8.1	3.4
50%	4.7	7.7	2.0	6.1	7.5	2.2	5.4	7.9	2.5	6.6	7.0	2.5	5.8	7.7	2.4	6.1	7.8	2.6
60%	4.4	7.8	2.0	6.0	7.5	2.0	5.4	8.1	2.2	5.4	6.8	2.0	5.3	7.0	2.1	5.8	7.5	3.0
70%	4.5	7.7	2.0	5.4	7.5	1.7	5.3	7.1	2.2	5.2	6.9	1.6	5.2	6.5	1.9	5.0	7.3	2.4
80%	3.9	7.7	1.8	5.1	7.2	1.6	5.0	6.7	1.8	4.9	7.3	1.8	5.0	6.8	1.7	5.3	7.3	2.4
90%	4.4	7.5	1.8	5.2	7.2	1.5	4.5	6.7	2.0	4.6	7.3	1.8	4.6	6.6	1.9	5.5	7.5	2.9

All values are indicated in mm.
RO, right cranial ostium; CDO, caudodorsal ostium; LO, left cranial ostium.

Table 12. Comparison of the mean pulmonary vein (PV) ostial diameter between the ventricular end-systole (30-40% R-R interval) and ventricular end-diastole (0%, 70-90% R-R interval) in six cats.

	End-diastole (mm)	End-systole (mm)	*p*-value
RO	4.875±0.404593	5.775±0.580165	0.000
CDO	7.17917±0.330979	7.96667±0.283912	0.000
LO	1.94167±0.320213	2.44167±0.412219	0.000

All values are expressed as means ± standard deviations. There was a significant difference between ventricular end-systole and ventricular end-diastole in all PV ostia ($p<0.05$).
PV, pulmonary vein; RO, right cranial ostium; CDO, caudodorsal ostium; LO, left cranial ostium.

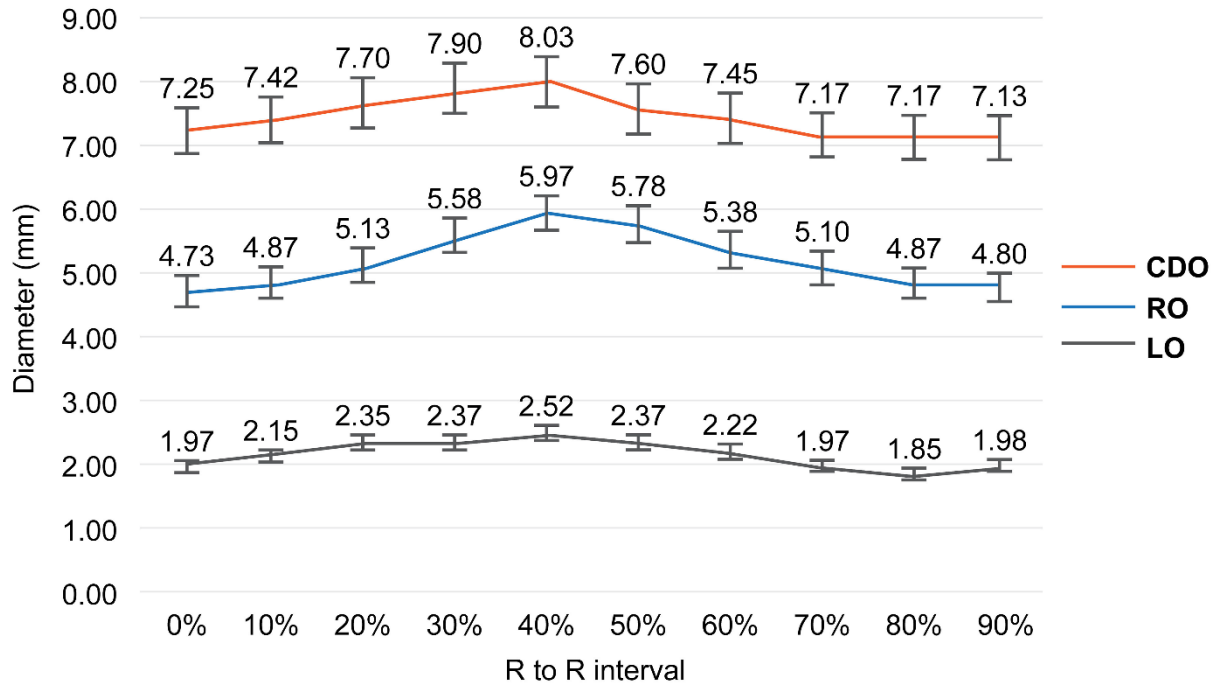

Figure 18. Variation of each pulmonary vein (PV) ostial diameter during the cardiac cycle in this study. This figure shows the mean value of each PV ostial diameter according to the cardiac cycle in six cats. All PV ostia show the maximum diameter at ventricular end-systole (40% R-R interval) and the minimum diameter at ventricular end-diastole (0%, 90% R-R interval). RO; right cranial ostium, CDO; caudodorsal ostium, LO; left cranial ostium

3.4 Discussion

The findings of this study indicate that the diameter variations of all PV ostia in cats according to the cardiac cycle could be successfully identified on ECG-gated CT images obtained using the new (modified) cardiac CT protocol implemented in Chapter 2. As in humans, the maximal diameter of each PV ostium corresponded to the end of ventricular systole, and the minimal diameter was measured in the end of ventricular diastole. Furthermore, this study showed significant differences in each of the three PV ostia enlarged at the end of ventricular systole compared with those at the end of ventricular diastole. In humans, the right superior PV ostium was found to be the largest and the right inferior PV ostium was the smallest, with the greatest dimensional change in the superior PV compared with the inferior PV, and the left superior PV exhibiting the greatest change (Manghat *et al.*, 2012). However, in our feline study, the diameter of the CDO was the largest and that of the LO was the smallest. In addition, the diameter change at the RO and CDO was larger than that of the LO. These anatomical differences suggest that further extensive studies are needed to determine the difference between humans and cats in the effect of PV function as well as the pathophysiology of atrial fibrillation associated with the extent and degree of myocardial sleeve at each PV ostium, and pulmonary congestion or edema.

PV blood flow is typically biphasic: the first phase occurs during ventricular systole and the second during ventricular diastole (Choi *et al.*, 2005; Manghat *et al.*, 2012). The PV orifice area also changes considerably during the cardiac cycle (Manghat *et al.*, 2012). During ventricular systole, blood flows from the PVs into the LA upon closure of the mitral valve. This is driven by left ventricular long-axis shortening,

which lengthens the LA, thus, increasing the pressure gradient between the PV and LA, and in effect, "pulls" blood into the LA (Manghat *et al.*, 2012). During early diastole, while blood is flowing into the left ventricular chamber, there is a drop in LA pressure and blood is passively pulled into the LA as it moves through the mitral valve into the left ventricular chamber. By mid to end ventricular diastole, the PV pressure equalizes with ventricular diastolic pressure, because of which antegrade PV flow begins to cease.

In small animal clinics, clinicians routinely evaluate the relative size of the PV and PA on radiographs by comparing them to the size of the ribs (Birettoni *et al.*, 2016). However, radiographic examination may vary depending on the breed, age, obesity, and underlying thoracic disease. In addition, the PV-to-PA ratio using echocardiography has been suggested as a predictive factor for discriminating healthy or subclinical patients with cardiomyopathy and patients with congestive heart failure in dogs and cats (Merveille *et al.*, 2015; Birettoni *et al.*, 2016; Patata *et al.*, 2020). In a feline study, healthy and subclinical cats did not differ in the PV-to-PA ratio in the echocardiography; meanwhile, cats with congestive heart failure had a larger ratio compared with healthy and subclinical cats (Patata *et al.*, 2020). In accordance with a previous study, our data also showed that the PV ostial diameter in one subclinical HCM phenotype cat did not differ from that in the five normal cats, although the maximal diameter in the CDO and LO of one HCM phenotype cat was slightly larger than those of the five normal cats. However, considering several limitations in the echocardiographic examination, including the operator's technique, patient obesity, and patient's heart rate or respiration, the evaluation of all PV ostia using ECG-gated images obtained through a new (modified) cardiac CT protocol holds the potential to be valuable and useful in veterinary clinics in the future. An

additional limitation is that echocardiography can image only in the RO region and not all three PV ostia.

In this study, the PV drainage patterns of six cats showed three PV ostia, unlike humans who have four PV ostia, similar to a previous feline study (Panopoulos *et al.*, 2019). In humans, many studies have shown that the superior veins have longer myocardial sleeves than the inferior veins, with the left superior PV having the longest sleeve and the right inferior PV having the shortest (Manghat *et al.*, 2012). In this study, in all cats, the RO and LO had a long common trunk, and the CDO had a short common trunk. Although further studies should encompass histological examination, this study suggest the possibility that myocardial sleeves of the RO and LO are longer than that of the CDO and could be considered as a pathophysiology of atrial fibrillation.

Although studies in humans have reported that patients with an enlarged LA may have larger PVs than those with a normal-sized LA and the diameter of the left superior PV is significantly larger in men than in women, there is no significant correlation between the heart or LA size, sex, BW, age, and the PV ostial diameter in this feline study (Kim *et al.*, 2005; Cronin *et al.*, 2007). This may be attributed to a slightly larger LA/AO ratio (1.56) in one HCM phenotype patient than in the five normal cats and six cats showing normal mitral E flow on echocardiography. Therefore, although there was no statistical significance, further extensive research may be necessary for many populations with various degrees of LA/AO ratio or high mitral E flow. With these future studies, it may be clinically useful to establish new criteria for an early prediction or cut-off value of pulmonary congestion or pulmonary edema in patients with early stages of the various heart diseases.

As previously mentioned, one limitation of our study was the small sample size.

Other limitations include the possibility of inaccurate PV ostial diameter measurement on MDCT as well as the lack of confirmation by biopsy or necropsy. Although our data could be sufficiently reliable in that we compared data from the same cross-section and showed significant differences between the ventricular end-systole and ventricular end-diastole in all PV ostia, further research is needed to measure the cross-sectional area using 3D imaging or vessel tracking in all PV ostia, because the diameter of each PV ostium by two-dimensional measurement is more susceptible to inaccuracies by shifting the imaging plane and choice of window width and level settings for display of the CT angiographic data, which can affect the measured vein diameter and cross sectional area. In addition, the volume measurement of each PV common trunk may be useful as an additional predictive factor for pulmonary congestion in the future. Finally, the risk of anesthesia can be significant, especially in animals with heart disease. Thus, difficulties in the practical application of MDCT imaging may also be considered.

Despite some limitations and the necessity of further research, this study suggests the clinical feasibility of using ECG-gated CT images to provide more detailed anatomical information on the PV, including dimensional changes during the cardiac cycle in cats, similar to that in humans. ECG-gated MDCT of the PVs may also be useful, because the non-invasive, easily reproducible nature and ability to demonstrate 3D anatomy are worthwhile advantages over other techniques. Based on this study, knowledge of variation in the PV ostium may offers interesting avenues for potential research into the effect of PV function in felines with atrial fibrillation and early detection of variable distribution of pulmonary congestion or edema in cats.

Consequently, the new (modified) cardiac CT protocol employed in this study demonstrated the potential to assess not only CA evaluation in Chapter 2 but also the

variations of the PV ostium throughout the cardiac cycle in this chapter. This suggests that the protocol has the capability to provide comprehensive imaging and evaluation of both CAs and PV ostia, expanding the diagnostic capabilities of cardiac CT in veterinary medicine.

General Conclusion

In conclusion, the new (modified) cardiac CT scan protocol presented in this study, which involves a combination of non-ECG-gated and ECG-gated scans without bolus tracking, has shown to be successful and valuable in cardiac imaging of both dogs and cats. The non-ECG-gated high-slice cardiac CT scan method demonstrated clinical utility by allowing evaluation of the main CAs (except the S branch) and potential diagnosis of CA anomalies in dogs. It also offers the benefit of imaging the CrVC, RVOT, and PAs in cats, providing visualization of the right heart circulation. On the other hand, the ECG-gated scan method proved advantageous in detecting small-sized lesions in the heart or pericardium in dogs and providing detailed anatomical information about the CAs and PV ostial changes during the cardiac cycle in cats. This modified scanning method has the potential to simultaneously evaluate the CrVC, RVOT, and PAs, along with the left heart and CAs. This comprehensive evaluation can be particularly beneficial in assessing patients with congenital cardiovascular anomalies such as PS or left persistent CrVC, allowing for a thorough assessment of both sides of the heart.

Furthermore, this new (modified) scan protocol may offer additional potential advantages, such as reducing anesthesia time and radiation exposure, and the ability to examine the abdomen or whole body using non-ECG-gated scan timing. The protocol has demonstrated its effectiveness in obtaining diagnostic images, providing comprehensive evaluation of cardiovascular structures, and facilitating the identification of important variations according to the cardiac cycle. Overall, the new

(modified) cardiac CT scan protocol holds promise as a reliable and practical tool for clinical application in veterinary medicine, supporting the assessment and management of various cardiovascular conditions in dogs and cats.

References

Auriemma E, Armienti F, Morabito S, Specchi S, Rondelli V, Domenech O, Guglielmini C, Lacava G, Zini E, Khouri T. Electrocardiogram-gated 16-multidetector computed tomographic angiography of the coronary arteries in dogs. Vet Rec, 2018; 183: 473.

Barszcz K, Kupczyńska M, Polguj M, Klećkowska-Nawrot J, Janeczek M, Goździewska-Harłajczuk K, Dzierzęcka M, Janczyk P. Morphometry of the coronary ostia and the structure of coronary arteries in the shorthair domestic cat. PLoS One, 2017; 12: e0186177.

Birettoni F, Caivano D, Patata V, Moïse NS, Guglielmini C, Rishniw M, Porciello F. Canine pulmonary vein-to-pulmonary artery ratio: Echocardiographic technique and reference intervals. J Vet Cardiol, 2016; 18: 326–335.

Bowden S, Winter RL, Hostnik ET, Habing A, Green E. Right coronary artery to left ventricle coronary cameral fistula in a cat. J Vet Cardiol, 2022; 44: 57–62.

Brewer FC, Moïse NS, Kornreich BG, Bezuidenhout AJ. Use of computed tomography and silicon endocasts to identify pulmonary veins with echocardiography. J Vet Cardiol, 2012; 14: 293–300.

Cao G, Chen W, Pan K, Sun H, Wang Z. Reduced artifacts and improved diagnostic value of 640-slice computed tomography in patients with cardiac pacemakers. J Int Med Res, 2019; 47: 1916-1926.

Chen YA, Nguyen ET, Dennie C, Wald RM, Crean AM, Yoo SJ, Jimenez-Juan L. Computed tomography and magnetic resonance imaging of the coronary sinus: anatomic variants and congenital anomalies. Insights Imaging, 2014; 5: 547−557.

Choi SI, Seo JB, Choi SH, Lee S-H, Do K-H, Ko SM, Lee JS, Song J-W, Song K-S, Choi K-J, Kim Y-H, Lim T-H. Variation of the size of pulmonary venous ostia during the cardiac cycle: optimal reconstruction window at ECG-gated multi-detector row CT. Eur Radiol, 2005; 15: 1441−1445.

Côté E, MacDonald KA, Meurs KM, Sleeper MM. Feline Cardiology. Chichester, UK: Wiley-Blackwell (2011). p. 103−109.

Cronin P, Kelly AM, Desjardins B, Patel S, Gross BH, Kazerooni EA, Morady F, Oral H, Carlos RC. Normative analysis of pulmonary vein drainage patterns on multidetector CT with measurements of pulmonary vein ostial diameter and distance to first bifurcation. Acad Radiol, 2007; 14: 178−188.

de Heer LM, Habets J, Chamuleau SAJ, Mali WPTM, van Herweren LA, Kluin J, Budde RPJ. Multidetector row computed tomography assessment of the

native aortic and mitral valve: a call for routine assessment of left-sided heart valves during coronary computed tomography. Cardiol Rev, 2012; 20: 222-229.

de Oliveira CLS, David GS, Carvalho MdO, Dornelas D, Araújo S, da Silva NC, Ruiz CR, Fernandes JR, Wafae N. Anatomical indicators of dominance between the coronary arteries of dogs. Int J Morphol, 2011; 29: 845–849.

Drees R, Frydrychowicz A, Keuler NS, Reeder SB, Johnson R. Pulmonary angiography with 64-multidetector-row computed tomography in normal dogs. Vet Radiol Ultrasound, 2011a; 52: 362–367.

Drees R, Frydrychowicz A, Reeder SB, Pinkerton ME, Johnson R. 64-multidetector computed tomographic angiography of the canine coronary arteries. Vet Radiol Ultrasound, 2011b; 52: 507-515.

Drees R, Francois CJ, Saunders JH. Invited review-computed tomographic angiography (CTA) of the thoracic cardiovascular system in companion animals. Vet Radiol Ultrasound, 2014; 55: 229-240.

Estrada APD, Lopes RdO, Villacorta H Jr. Coronary tortuosity and its role in myocardial ischemia in patients with no coronary obstructions. Int J Cardiovasc Sci, 2017; 30: 163–170.

Fernandez del Palacio MJ, Bayon A, Agut A. Dilated coronary sinus in a dog with persistent left cranial vena cava. Vet Radiol Ultrasound, 1997; 38: 376−379.

Gaibazzi N, Rigo F, Reverberi C. Severe coronary tortuosity or myocardial bridging in patients with chest pain, normal coronary arteries, and reversible myocardial perfusion defects. Am J Cardiol, 2011; 108: 973−978.

Gunther-Harrington, CT, Phillips KL, Visser LC, Fousse SL, Stern JA. Non-electrocardiographic-gated computed tomographic angiography can be used to diagnose coronary artery anomalies in bulldogs with pulmonary valve stenosis. Vet Radiol Ultrasound, 2019; 60: 38-46.

Habing A, Coelho JC, Nelson N, Brown A, Beal M, Kinns J. Pulmonary angiography using 16 slice multidetector computed tomography in normal dogs. Vet Radiol Ultrasound, 2011; 52: 173−178.

Hamabe A, Okuyama Y, Miyauchi Y, Zhou S, Pak H-N, Karagueuzian HS, Fishbein MC, Chen P-S. Correlation between anatomy and electrical activation in canine pulmonary veins. Circulation, 2003; 107: 1550−1555.

Hassani C, Saremi F. Comprehensive cross-sectional imaging of the pulmonary veins. RadioGraphics, 2017; 37: 1928−1954.

Heaney AM, Bulmer BJ. Cor triatriatum sinister and persistent left cranial vena

cava in a kitten. J Vet Intern Med, 2004; 18: 895–898.

Khosravani-Rudpishi M, Joharimoghadam A, Rayzan E. The significant coronary tortuosity and atherosclerotic coronary artery disease; what is the relation? J Cardiovasc Thorac Res, 2018; 10: 209–213.

Kim J, Kim S, Lee Y, Yoon H, Eom K. Contrast echocardiography in two-dimensional left ventricular measurements: comparison with 256-row multi-detector computed tomography as a reference standard in Beagles. J Vet Sci, 2019; 20: e45.

Kim J, Kim D-H, Jee H, Hwang J, Yoon J. Type B valvular and supravalvular pulmonic stenosis with aberrant pre-pulmonic right coronary artery diagnosed by non-ECG-gated, multislice computed tomography in a Boston terrier. J Vet Cardiol, 2021, 38: 12-17.

Kim YH, Marom EM, Herndon JE 2nd, McAdams HP. Pulmonary vein diameter, cross-sectional area, and shape: CT analysis. Radiology, 2005; 235: 43–49.

Laborda-Vidal P, Maddox TW, Navarro-Cubas X, Dukes-McEwan J, McConnell JF. Comparison between echocardiographic and non-ECG-gated CT measurements in dogs. Vet Rec, 2015; 176: 335.

Laborda-Vidal P, Pedro B, Baker M, Gelzer AR, Dukes-McEwan J, Maddox TW.

Use of ECG-gated computed tomography, echocardiography and selective angiography in five dogs with pulmonic stenosis and one dog with pulmonic stenosis and aberrant coronary arteries. J Vet Cardiol, 2016; 18: 418-426.

Lacomis JM, Goitein O, Deible C, Schwartzman D. CT of the pulmonary veins. J Thorac Imaging 2007; 22: 63-76.

Lee-Fowler TM, Cole RC, Dillon AR, Tillson DM, Garbarino R, Barney S. High-resolution computed tomography evaluation of the bronchial lumen to vertebral body diameter and pulmonary artery to vertebral body diameter ratios in anesthetized ventilated normal cats. J Feline Med Surg, 2017; 19: 1007–1012.

Lei Z, Fu Q, Shi H, Xu H, Han P, Yu J. The diagnostic evaluation of 640 slice computed tomography angiography in the diagnosis of coronary artery stenosis. Digit Med, 2015; 1: 67-71.

Letendre JA, Boysen S. Cranial vena cava syndrome secondary to cryptococcal mediastinal granuloma in a cat. Can Vet J, 2015; 56: 365–369.

Lye TH, Iyer V, Marboe CC, Hendon CP. Mapping the human pulmonary venoatrial junction with optical coherence tomography. Biomed Opt Express, 2019; 10: 434–448.

Manghat NE, Mathias HC, Kakani N, Hamilton MCK, Morgan-Hughes G,

Roobottom CA. Pulmonary venous evaluation using electrocardiogram-gated 64-detector row cardiac CT. Br J Radiol, 2012; 85: 965-971.

Merveille A-C, Bolen G, Krafft E, Roels E, Gomart S, Etienne A-L, Clercx C, Mc Entee K. Pulmonary vein-to-pulmonary artery ratio is an echocardiographic index of congestive heart failure in dogs with degenerative mitral valve disease. J Vet Intern Med, 2015; 29: 1502−1509.

Miller MW, Gordon SG, Saunders AB, Arsenault WG, Meurs KM, Lehmkuhl LB, Bonagura JD, Fox PR. Angiographic classification of patent ductus arteriosus morphology in the dog. J Vet Cardiol, 2006; 8: 109-114.

Nagpal P, Agrawal MD, Saboo SS, Hedgire S, Priya S, Steigner ML. Imaging of the aortic root on high-pitch non-gated and ECG-gated CT: awareness is the key!. Insights Imaging, 2020; 11: 51.

Noestelthaller A, Probst A, König HE. Branching patterns of the left main coronary artery in the dog demonstrated by the use of corrosion casting technique. Anat Histol Embryol, 2007; 36: 33−37.

Owens EJ, Scollan KF, Pereyda TX, LeBlanc NL. Single left coronary ostium with a prepulmonic right coronary artery course in a French Bulldog with congenital valvular pulmonary stenosis. J Vet Cardiol, 2021; 36: 1-5.

Panopoulos I, Auriemma E, Specchi S, Diana A, Pietra M, Papastefanou A, Zini E,

Cipone M. 64-multidetector CT anatomical assessment of the feline bronchial and pulmonary vascular structures. J Feline Med Surg, 2019; 21: 893-901.

Patata V, Caivano D, Porciello F, Rishniw M, Domenech O, Marchesotti F, Giorgi ME, Guglielmini C, Poser H, Spina F, Birettoni F. Pulmonary vein to pulmonary artery ratio in healthy and cardiomyopathic cats. J Vet Cardiol, 2020; 27: 23–33.

Pelliccia F, Cecchi F, Olivotto L, Camici PG. Microvascular dysfunction in hypertrophic cardiomyopathy. J Clin Med, 2022; 11: 6560.

Piffer CR, Piffer MI, Santi FP, Dayoub MC. Anatomic observations of the coronary sinus in the dog (Canis familiaris). Anat Histol Embryol, 1994; 23: 301–308.

Punzo B, Forte E, Salvatore M, Cavaliere C, Cademartiri F. Case report of coronary artery fistula: added value of multimodal advanced imaging with cardiac computed tomography and cardiac magnetic resonance. Medicine (Baltimore), 2019; 98: e18255.

Ratajczak P, Sławińska A, Martynowska-Rymer I, Strześniewski P, Rusak G. Anatomical evaluation of the pulmonary veins and the left atrium using computed tomography before catheter ablation: reproducibility of measurements. Pol J Radiol, 2016; 81: 228–232.

Reid LE, Dillon AR, Hathcock JT, Brown LA, Tillson M, Wooldridge AA. High-resolution computed tomography bronchial lumen to pulmonary artery diameter ratio in anesthetized ventilated cats with normal lungs. Vet Radiol Ultrasound, 2012; 53: 34–37.

Saulnier DC. Imaging of the canine heart using non-ECG-gated 16 and ECG-gated 64 multidetector row computed tomography [MS Thesis]. Blacksburg, VA: Virginia Polytechnic Institute and State University, 2012.

Scansen BA. Coronary artery anomalies in animals. Vet Sci, 2017; 4: 20.

Schrope DP. Primary pulmonic infundibular stenosis in 12 cats: natural history and the effects of balloon valvuloplasty. J Vet Cardiol, 2008; 1: 33-43.

Shah SS, Teague SD, Lu JC, Dorfman AL, Kazerooni EA, Agarwal PP. Imaging of the coronary sinus: normal anatomy and congenital abnormalities. RadioGraphics, 2012; 32: 991–1008.

Stieger-Vanegas SM, Scollan KF, Riebold TW. Evaluation of non-ECG and ECG-gated computed tomographic angiography for three-dimensional printing of anomalous coronary arteries in dogs with pulmonic stenosis. J Vet Cardiol, 2019; 26: 39-50.

Sun Z. Cardiac CT imaging in coronary artery disease: Current status and future

direction. Quant Imaging Med Surg, 2012; 2: 98-105.

Taron J, Foldyna B, Eslami P, Hoffmann U, Nikolaou K, Bamberg F. Cardiac computed tomography—more than coronary arteries? A clinical update. Rofo, 2019; 191: 817-826.

To A, Hostnik ET, Rhinehart JD, Scansen BA. Electrocardiography-gated cardiac CT angiography can differentiate brachycephalic dogs with and without pulmonary valve stenosis and findings differ from transthoracic echocardiography. Vet Radiol Ultrasound, 2019; 60: 145-158.

Visser LC, Scansen BA, Schober KE. Single left coronary ostium and an anomalous prepulmonic right coronary artery in 2 dogs with congenital pulmonary valve stenosis. J Vet Cardiol, 2013; 15: 161-169.

Wagner M, Butler C, Rief M, Beling M, Durmus T, Huppertz A, Voigt A, Baumann G, Hamm B, Lembcke A, Vogtmann T. Comparison of non-gated vs. electrocardiogram-gated 64-detector-row computed tomography for integrated electroanatomic mapping in patients undergoing pulmonary vein isolation. Europace, 2010; 12: 1090-1097.

국문초록

개와 고양이에서 변형된 컴퓨터 단층촬영 프로토콜의 임상적 평가

서울대학교 대학원

수의학과 임상수의학 전공

김 준 영

인의에서는 기존의 침습적 혈관 조영술을 대신하여 다중 슬라이스 심장 컴퓨터 단층 촬영이 비침습적인 심혈관계 평가의 표준이 되고 있다. 수의학에서는 2011년부터 비심전도 동기 또는 심전도 동기 심장 컴퓨터 단층 촬영을 이용한 개 심혈관계 평가가 보고되었으나, 충분한 임상 적용과 연구가 부족한 상황이다. 또한, 고양이에서도 비심전도 동기 혹은 심전도 동기 심장 컴퓨터 단층촬영을 이용한 임상적 적용과 연구가 필요할 수 있다. 이전의 개 연구들은 비심전도 동기 촬영 방법보다 심전도 동기 촬영 방법이 심장 운동에 의한 아티팩트를 최소화할 수 있어 심장 및 관상동맥에 대한 세부적인 영상화에 더욱 효과적이라고 보고해왔다. 하지

만 소동물들은 심박수가 빠르고 심박수 감소를 위한 베타 차단제 약물이 효능을 보기 어려울 수 있어 심전도 동기 방법을 수행하기 어려울 수 있다. 따라서 비심전도 동기 및 심전도 동기 다중 슬라이스 심장 컴퓨터 단층촬영 영상의 특징과 차이점, 제한점들을 이해하는 것이 필요하다. 수의학에서 비심전도 동기와 심전도 동기 다중 슬라이스 컴퓨터 단층 촬영의 임상적 유용성을 직접적으로 비교하는 것이 도움이 될 수 있다. 따라서, 본 연구는 비심전도 동기 방법의 임상 적용 가능성과 한계, 그리고 심전도 동기 영상만을 사용하는 장점을 조사하기 위해 실시되었다. 이는 두 가지 방법을 동시에 개와 고양이에게 적용하여 이루어질 수 있다. 이 연구의 궁극적인 목표는 개와 고양이에서 향후 활용할 수 있는 적절한 다중 슬라이스 심장 컴퓨터 단층촬영 프로토콜을 확립하는 것이다.

제1장에서는 6마리의 개 (동맥관 개존증 2마리, 심첨부 종양 2마리, 심막중피종 1마리, 정상 1마리)를 대상으로 160 슬라이스 컴퓨터 단층 촬영 장비를 이용한 비심전도 동기 및 심전도 동기 방법을 동시에 적용하였다. 5초 간격으로 총 5회의 비심전도 동기 촬영 후, bolus tracking 없이 연속적으로 retrospective 심전도 동기 촬영을 실시하였다. 세부적인 관상동맥 영상화에 적절한 비심전도 동기 촬영 시기와 심전도 동기 R-R 구간을 결정하고 선택된 영상에서 주요 관상동맥 가지들에 대한 시각적 평가를 하였다. 시각적 평가는 주관적인 방법으로 4단계로 등급을 결정하였다. 또한, 좌측 관상동맥 분지 패턴을 평가하였으며 심장 또는 심막 종양이 있는 개에서는 비심전도 동기 및 심전도 동기 영상에서 병변의 크기와 경계면 등 형태학적 평가를 비교하였다. 최적의 관상동맥 영상화를

보이는 비심전도 동기 촬영 시기와 심전도 동기 R-R 구간은 각각 두번째 촬영 시기와 심실 이완기 말기 (R-R 구간의 70-90%)로 확인되었다. 비심전도 동기 영상은 관상동맥에 대한 시각적 평가에서 5 kg 이하 개들의 septal 가지를 제외한 모든 주요 관상동맥 가지에서 높은 등급의 시각적 평가를 보였으며 심전도 동기 영상과 유의적인 차이를 보이지 않았다. 병변의 형태학적 평가에서는 두 마리 개에서 작은 크기의 심장 및 심막 병변들이 비심전도 동기 영상에 비해 심전도 동기 영상에서 명확하게 확인되었다. 본 연구는 비심전도 동기 다중 슬라이스 심장 컴퓨터 단층촬영 방법이 개의 주요 관상동맥을 평가할 수 있는 능력을 보여준다. 그러나, 심장이나 심막의 작은 병변을 식별하는 데는 비심전도 동기 방법보다 심전도 동기 방법을 선호해야 함을 시사한다.

제2장에서는 제1장과 동일한 심장 컴퓨터 단층 촬영 방법을 적용하여 고양이 관상동맥을 평가하고자 실시되었다. 스캔 타이밍에 따른 5회 연속 비심전도 동기 심장 컴퓨터 단층촬영 영상들의 특징들이 묘사되었다. 총 6마리 (정상 5마리, 비대성 심근증 1마리) 고양이가 연구에 포함되었다. 적절한 관상동맥 영상화를 보이는 비심전도 동기 촬영 시기와 심전도 동기 R-R 구간을 선택하였으며 선택된 영상에서 주요 관상동맥 가지들에 대한 시각적 평가를 하였다. 시각적 평가는 제1장과 동일한 방법으로 4단계로 등급을 결정하였다. 또한, 관상동맥 우세성과 좌측 관상동맥 분지 유형을 평가하였으며 각 관상동맥 가지들의 직경과 길이를 체중, 성별, 심장 VHS와 상관관계를 평가하였다. 비심전도 동기 방법에서 첫 번째 촬영 영상은 모든 고양이의 전대정맥, 우심실 배출로, 폐동맥의 명

확한 영상화를 보여주었다. 그러나, 좌측 심장과 관상동맥 영상화에는 어려움이 있었다. 두 번째 촬영 영상은 좌측 심장과 관상동맥의 영상화에 가장 적합한 것으로 확인되었으나, 심한 움직임 아티팩트로 관상 동맥 ostium과 근위 가지에 대한 영상화만 가능하였다. 세 번째 촬영 영상에서 좌측 심장과 관상동맥의 영상화 정도는 두 번째 촬영보다 낮았다. 네 번째와 다섯 번째 촬영 영상은 조영제의 배출로 평가할 수 없었다. 반면, 심전도 동기 영상에서는 관상동맥의 시각화가 양호 혹은 우수하였고, 이완기 말기에 상세한 주행 양상을 보였다. 이러한 영상들은 모든 고양이에서 비심전도 동기 촬영 영상보다 유의하게 우수한 결과를 보였다. 추가적으로, 다양한 패턴의 관상동맥 우세성과 좌측 관상동맥 분지 유형을 확인할 수 있었다. 관상동맥 길이와 직경은 체중 및 성별과는 유의적인 상관관계를 보이지 않았으나, 심장 VHS는 우측 관상동맥 길이와 양의 상관관계를, 좌측 주 관상동맥 길이와 음의 상관관계를 보였다. 결론적으로, 본 연구의 새로운 (변형된) 심장 컴퓨터 단층촬영 프로토콜은 모든 고양이에서 성공적으로 수행되었다. 이 촬영 방법은 전대정맥, 우심실 배출로, 폐동맥과 더불어 좌측 심장과 관상동맥에 대한 동시 평가에 유익할 수 있다고 판단된다. 이 변형된 방법은 양측 심장에 대한 종합적 평가를 통해 폐동맥 협착증이나 좌측 영속성 전대정맥과 같은 선천성 심혈관 이상을 가진 환자들의 평가에 도움이 될 수 있을 것이다.

제3장에서는 심장 주기 동안 폐정맥 ostium의 직경 변화를 확인하고, 새로운 (변형된) 심장 컴퓨터 단층촬영 프로토콜로 구현된 심전도 동기 영상의 장점을 평가하기 위해 설계되었습니다. 심전도 동기 영상으로 고양

이 폐정맥 ostium 수와 배출 패턴, 심장 주기에 따른 고양이 폐정맥 ostium의 직경 변화 확인과 심장 및 좌심방 크기와 폐정맥 ostium 직경과의 상관관계를 알아보기 위해 제 2장에서의 심전도 동기 영상을 후향적으로 분석하였다. 폐정맥 ostium은 right cranial ostium, left cranial ostium, caudodorsal ostium 등 총 3개의 ostium이 두 가지 패턴으로 좌심방으로 유출되는 것이 확인되었으며, 심장 주기에 따라 모든 폐정맥 ostium의 직경 변화가 확인되었다. 각 폐정맥 ostium의 최대 직경은 심실 수축기 말기에, 최소 직경은 심실 이완기 말기에 확인되었다. 통계 분석에서도 심실 수축기 말기와 이완기 말기 사이에 폐정맥 ostium의 유의적인 직경 차이가 있음을 확인하였다 ($p<0.05$). 심장 및 좌심방 크기와 3개의 폐정맥 ostium 직경 사이에서 유의적인 상관관계는 확인되지 않았다 ($p>0.05$). 제3장 연구를 통해 심장 주기 따른 고양이 폐정맥 ostium 직경 변화를 포함한 세부적인 폐정맥 해부학 정보를 제공하는 데 있어 심전도 동기 심장 컴퓨터 단층 촬영 영상의 유용성을 확인할 수 있었다. 이번 연구는 향후 고양이 폐정맥 ostium과 다양한 패턴의 폐수종 및 심방 세동 발병에 미치는 영향에 대한 지속적인 연구 방향성에 대한 가능성을 제공해 준다. 또한, 향후 수의 임상에서도 폐정맥 평가를 통한 radiofrequency ablation 등의 중재적 시술에 대한 임상 적용 가능성도 높여 줄 수 있을 것으로 생각된다. 이번 연구는 새로운 (변형된) 심장 컴퓨터 단층촬영 프로토콜로 얻어진 심전도 동기 영상만을 활용하는 이점을 보여주며, 심장 주기에 따른 폐정맥 ostium 변화에 대한 증거를 제공한다.

결론적으로, 이번 새로운 (변형된) 심장 컴퓨터 단층촬영 방법인 비심전

도 동기 촬영 후 bolus tracking 없이 심전도 동기 촬영하는 방법은 개와 고양이에서 성공적으로 수행되었으며, 방사선 노출과 마취 시간을 줄일 수 있는 잠재적인 장점을 보여준다. 비심전도 동기 다중 슬라이스 심장 컴퓨터 단층촬영 방법은 개의 주요 관상동맥을 평가하는 임상적 유용성을 보여준다. 또한, 전대정맥, 우심실 배출로, 폐동맥의 영상화를 혼합함으로써 폐동맥 협착증이나 좌측 영속성 전대정맥과 같은 선천성 심혈관 질환을 가진 환자들의 양측 심장 평가에 도움을 줄 수 있다. 추가적으로, 심전도 동기 촬영 방법은 심장이나 심막의 작은 병변 확인과 고양이의 관상동맥 평가 및 심장 주기 동안 폐정맥 ostium의 변화를 평가하는 데 장점을 제공해줄 수 있다. 전반적으로, 이번 새로운 (변형된) 심장 컴퓨터 단층촬영 프로토콜은 수의학 분야에서 임상 적용을 위한 신뢰성 있고 실용적인 도구로서의 가능성을 갖고 있으며, 개와 고양이의 다양한 심혈관 질환의 평가와 관리에 도움을 줄 수 있다.

주요어: 심전도, 컴퓨터 단층촬영, 관상동맥, 심막, 폐정맥, 심장 주기

학 번: 2018-38660